# Spectral modelling for passive scalar dynamics in homogeneous anisotropic turbulence

Antoine Briard, Thomas Gomez, Claude Cambon

# Spectral modelling for passive scalar dynamics in homogeneous anisotropic turbulence

**A. Briard [1] , T. Gomez [2] † and C. Cambon [3]**

[1] $\partial$'Alembert, CNRS UMR 7190, 4, Place Jussieu 75252 Paris Cedex 5, France

[2] USTL, LML, F-59650 Villeneuve d'Ascq, France

[3] Laboratoire de Mécanique des Fluides et d'Acoustique, Ecole Centrale de Lyon, France

(Received 6 January 2016; revised 13 May 2016; accepted 25 May 2016 - Vol 799, 159-199)

The present work aims at developing a spectral model for a passive scalar field and its associated scalar flux in homogeneous anisotropic turbulence. This is achieved using the paradigm of eddy-damped quasi-normal markovian (EDQNM) closure extended to anisotropic flows. In order to assess the validity of this approach, the model is compared to several detailed DNS and experiments of shear-driven flows and isotropic turbulence with a mean scalar gradient at moderate Reynolds numbers. This anisotropic modelling is then used to investigate the passive scalar dynamics at very high Reynolds numbers. In the framework of homogeneous isotropic turbulence submitted to a mean scalar gradient, decay and growth exponents for the cospectrum and scalar energies are obtained analytically and assessed numerically thanks to EDQNM closure. With the additional presence of a mean shear, the scaling of the scalar flux and passive scalar spectra in the inertial range are investigated and confirm recent theoretical predictions. Finally, it is found that in shear-driven flows, the small scales of the scalar second-order moments progressively return to isotropy when the Reynolds number increases.

**Key words:** Homogeneous Turbulence, Anisotropy, Passive Scalar

## 1. Introduction

The study of a passive scalar, such as small temperature fluctuations $\theta$, convected by a turbulent velocity field $u_i$, is of interest for several reasons. From a fundamental point of view; though homogeneous anisotropic turbulence (HAT) has been at the center of many theoretical, numerical and experimental works for almost 40 years, numerous questions still remain without clear answers. How do the energy, mainly produced at large scales by mean velocity and scalar gradients, affect the small scales dynamics? Is there a complete return to isotropy of small scales? Is the growth or decay dynamics of quantities, such as the kinetic energy and the scalar variance, predictable?

Upstream to these fundamental questions, there are practical reasons to the investigation of HAT. Indeed, taking into account anisotropy created by non-zero mean fields is an important feature to describe real flows by comparison to the classical case of homogeneous and isotropic turbulence (HIT). Notably, the deep understanding of homogeneous turbulence dynamics could provide further insights into the analysis of high Reynolds numbers natural flows such as atmospheric and oceanic ones. Such flows are complex

† Email address for correspondence: thomas.gomez@univ-lille1.fr

for multiple reasons, one being that their Reynolds numbers are much higher than the ones currently reachable in direct numerical simulations (DNS) and experiments. For instance, the Reynolds number based on the Taylor micro-scale $Re_\lambda = K\sqrt{20/3\nu\epsilon}$ - where $K =< u_i u_i > /2$ is the kinetic energy, $\epsilon = \nu < \partial_j u_i \, \partial_j u_i >$ its dissipation rate, $u_i$ the fluctuating velocity, and $\nu$ the kinematic viscosity - can be of order $10^4$ in atmospheric flows. Such large Reynolds numbers simulations without modelling would require huge computational resources to capture only the early stage of the dynamics, and would need a fine description of all scales, from the most energetic ones to the dissipative ones at the level of the Kolmogorov scale $\eta = (\epsilon/\nu^3)^{-1/4}$. In addition to very high Reynolds numbers involved in atmospheric flows, the nature itself of such flows is complex as it contains many different physical phenomena. Indeed, a fine description of atmospheric dynamics would require to take into account rotation, helicity, stratification, shear, and mean scalar gradient from the ground to high altitude (Wyngaard & Coté 1972; Kader & Yaglom 1991). Mean velocity and scalar gradients are also deeply associated to production mechanisms in the turbulence dynamics regardless of the flow type. Indeed, they play a fundamental role in the energy transfers through scales. Therefore, insights concerning the role of mean velocity or scalar gradients are of great interest for turbulent flows, and specifically the ones where departure from isotropy is generated by anisotropic forces or by solid walls giving rise to shearing stresses. Moreover, a better understanding of all these anisotropic turbulent flows could be obtained by making separate investigations of isolated mechanisms at high Reynolds numbers, which are still quite unreachable using DNS.

This is the approach followed in this study. In order to achieve this objective, notably for very high Reynolds numbers, the dynamics of a passive scalar field $\theta$ and its flux $< u_i\theta >$ in HAT is addressed with the use of an eddy-damped quasi-normal Markovian (EDQNM) closure adapted to anisotropic flows. The modelling proposed here is an extension to the scalar case of a model recently developed by Mons *et al.* (2016). The purpose of this work is therefore twofold: developing the theoretical basis of an anisotropic EDQNM modelling for the passive scalar, and using it to investigate non-helical high Reynolds numbers turbulence. Moreover, the present model is developed for arbitrary mean velocity gradients that produce energy: consequently it is not adapted to the case of purely rotating turbulence in which there is no energy production and where the dynamics is dominated by dispersive (inertial) waves interacting non-linearly, requiring even more complex tools (Cambon & Jacquin 1989; Sagaut & Cambon 2008). The emphasis is thus put on three different configurations: Homogeneous Isotropic Turbulence with a mean Scalar Gradient (HITSG), Homogeneous Shear Turbulence (HST), and finally, these two frameworks are combined into Homogeneous Shear Turbulence with mean Scalar Gradient (HSTSG) as notably encountered in atmospheric flows.

In HITSG, the mean scalar gradient $\Lambda = d\Theta/dx_3$, where $\Theta$ is the mean scalar field, produces scalar fluctuations so that the scalar variance $K_T =< \theta^2 >$ can increase whereas the isotropic velocity field is decaying. This mean scalar gradient creates an anisotropic flux $< u_3\theta >$, called the cospectrum in spectral space, which has received a lot of attention: with spectral closures (Herr *et al.* 1996; O'Gorman & Pullin 2003; Bos *et al.* 2004, 2005; O'Gorman & Pullin 2005), with DNS (Pumir 1994; Overholt & Pope 1996), theoretically (Lumley 1967), and experimentally (Venkataramani & Chevray 1978; Warhaft 1980; Sirivat & Warhaft 1983; Jayesh & Warhaft 1992; Mydlarski & Warhaft 1998; Mydlarski 2003). In all these studies, the scaling of the cospectrum is uncertain in the inertial range, $k^{-7/3}$ or $k^{-2}$, probably because of too low Reynolds numbers. This point will be addressed hereafter.

The case of a mean velocity gradient $S = dU_1/dx_3$, where $U_i$ is the mean velocity field, without mean scalar gradient, has been less studied: a rapid decrease of $K_T$ was observed

experimentally (Warhaft 1980; Karnik & Tavoularis 1989), and this has been confirmed theoretically (Gonzalez 2000). Interestingly, in such a configuration, the evolution of the passive scalar field dynamics is completely different from the one of the velocity field.

Finally, when both mean velocity and scalar gradients are applied, there is a continuous production of kinetic energy $K(t)$ that grows exponentially for large dimensionless times $St$. Consequently, thanks to interactions with the scalar flux, $K_T$ grows exponentially as well. The HSTSG configuration has been at the center of many works as well: with a classical EDQNM approach (Bos & Bertoglio 2007), with DNS (Shirani *et al.* 1981; Rogers *et al.* 1989; Brethouwer 2005; Kassinos *et al.* 2007) and experimentally (Tavoularis & Corrsin 1981; Danaila *et al.* 1999; Ferchihi & Tavoularis 2002). Even without rotation, the HSTSG configuration remains quite representative of atmospheric flows (Wyngaard & Coté 1972).

Besides, the small scales return to isotropy (RTI) for each of the three cases presented is of primary importance: indeed, according to Kolmogorov (1941), small scales of the flow should return to isotropy whatever the large scales are. While the small scales RTI of second-order moments of the velocity field is well-admitted (Speziale *et al.* 1990; Pumir 1996; Garg & Warhaft 1998; Shen & Warhaft 2000), the case of third-order moments (such as the derivative skewness of the velocity in shear flows) is still an open question. Moreover, it appeared that the scalar case is even more complicated, since the conclusion is not clear regarding second-order moments: departure from isotropy are observed experimentally and numerically at small scales with a mean scalar gradient only, in shear-driven flows, in boundary layers and in jets (Sreenivasan *et al.* 1979; Sreenivasan & Tavoularis 1980; Sreenivasan 1991; Pumir 1994; Danaila *et al.* 1999). Consequently, and in order to clarify the return to isotropy of the scalar small scales, high Reynolds numbers anisotropic flows will be investigated thanks to the present modelling.

The general method used to develop the present model, briefly called *anisotropic EDQNM*, is now described. Firstly, the dynamical equations that govern the evolution of the spectral second-order correlations, referred to as Craya equations, are considered. They have an exact part, linear and closed, which corresponds to mean gradient effects. The second part, originating from triple correlations contributions is explicitly closed with EDQNM. The closure technique for anisotropic flows is discussed in several papers, with a complete survey in Sagaut & Cambon (2008): for the sake of simplicity, explicit effects of mean velocity and scalar gradients are not taken into account in the equations for three-point third-order correlations. Such effects are important only in the case of interacting waves, as in rotating turbulence (Cambon & Jacquin 1989) and can be globally modelled, without altering the structure of the EDQNM model, as in Burlot *et al.* (2015) for unstably stratified turbulence. The latter study shows the strong analogy between shear-driven flows with passive scalar and stratified buoyant flows, in which the buoyancy fluctuation (density or temperature) is an active scalar. In a second step, a tractable model is obtained in terms of spherically-averaged descriptors, so that the state vector depends only on the wavenumber modulus $k$: the integration on spherical shells is performed analytically. This procedure in two steps generalizes the pioneering work of Cambon *et al.* (1981) for the velocity field, and consistently extends the recent model by Mons *et al.* (2016) to the scalar and velocity-scalar correlations modelling.

This method is applied to model the dynamics of the scalar field and of the mixed velocity-scalar correlation in HAT. The closure is presented in §2 and §3, along with the main equations and the anisotropic EDQNM modelling: the evolution equations of the passive scalar and the scalar flux constitute one of the main results of this study. §4 is devoted to the validation of the present model, where several detailed comparisons with experimental and numerical works are proposed at moderate Reynolds numbers. Then,

new numerical and theoretical results at very high Reynolds numbers are presented in §5. Finally, §6 is dedicated to the main conclusions of the present work and perspectives.

## 2. Closed equations for the passive scalar and scalar flux

In this section, incompressible homogeneous turbulence without rotation and helicity is considered. The evolution equations of the spectral kinetic and scalar second-order correlations are derived. Then, the closure method for the non-linear terms is presented along with the EDQNM approximation. In what follows, time-dependence will sometimes be omitted for a better readability.

### 2.1. *Brief overview of the velocity field*

In this part, the main theoretical aspects of Mons *et al.* (2016) are recalled for the sake of clarity and to introduce important notations. The spectral velocity second-order correlation - or spectral Reynolds stress tensor - is defined as

$$\hat{R}_{ij}(\boldsymbol{k},t)\delta(\boldsymbol{k}-\boldsymbol{p}) =< \hat{u}_i^*(\boldsymbol{p},t)\hat{u}_j(\boldsymbol{k},t) >, \tag{2.1}$$

where $< . >$ is an ensemble average, $()^*$ the complex conjugate, and $\boldsymbol{k}$ and $\boldsymbol{p}$ are wave vectors of modulus the wavenumbers $k$ and $p$. $\hat{()}$ denotes the Fourier transform and $\hat{u}_i$ is the spectral fluctuating velocity. $\hat{R}_{ij}$ corresponds to $R_{ij} =< u_i u_j >$ in physical space, and its evolution equation in the presence of a mean velocity gradient $A_{ij} = dU_i/dx_j$ is called the Craya equation and reads

$$\left(\frac{\partial}{\partial t} - A_{ln}k_l\frac{\partial}{\partial k_n} + 2\nu k^2\right)\hat{R}_{ij}(\boldsymbol{k}) + M_{in}(\boldsymbol{k})\hat{R}_{nj}(\boldsymbol{k}) + M_{jn}(\boldsymbol{k})\hat{R}_{ni}(\boldsymbol{k}) = T_{ij}^{NL}(\boldsymbol{k}), \tag{2.2}$$

where $\nu$ is the kinematic viscosity, $M_{ij}(\boldsymbol{k}) = (\delta_{in} - 2\alpha_i\alpha_n)A_{n_j}$, with $\alpha_i = k_i/k$. $T_{ij}^{NL}$ is the total non-linear transfer which can be split into a conservative part and a non-conservative one, the latter being linked to slow-pressure terms and thus responsible for the return to isotropy (RTI) mechanism. The kinetic energy and its dissipation rate are defined as

$$K(t) = \frac{R_{ii}(t)}{2} = \int_0^\infty E(k,t)dk, \qquad \epsilon(t) = 2\nu\int_0^\infty k^2E(k,t)dk = \nu < \frac{\partial u_i}{\partial x_j}\frac{\partial u_i}{\partial x_j} > ,$$

where $E(k,t)$ is the kinetic energy spectrum. In what follows, the $\mathcal{E}$-$Z$ decomposition is used (Cambon & Rubinstein 2006) for a flow without helicity

$$\hat{R}_{ij}(\boldsymbol{k}) = \underbrace{\frac{E(k)}{4\pi k^2}P_{ij}(\boldsymbol{k})}_{\hat{R}_{ij}^{(iso)}(\boldsymbol{k})} + \underbrace{\left(\mathcal{E}(\boldsymbol{k}) - \frac{E(k)}{4\pi k^2}\right)P_{ij}(\boldsymbol{k})}_{\hat{R}_{ij}^{(dir)}(\boldsymbol{k})} + \underbrace{\Re\Big(Z(\boldsymbol{k})N_i(\boldsymbol{k})N_j(\boldsymbol{k})\Big)}_{\hat{R}_{ij}^{(pol)}(\boldsymbol{k})}, \tag{2.3}$$

where $\Re()$ denotes the real part. $\mathcal{E} - E/(4\pi k^2)$ reflects directional anisotropy, *i.e.* the difference between the energy in a given direction and the spherical average, and is linked to the kinetic energy spectrum through an integral on a spherical surface $S_k$ of radius $k$

$$E(k,t) = \int_{S_k}\mathcal{E}(\boldsymbol{k},t)\,d^2\boldsymbol{k} = \frac{1}{2}\int_{S_k}\hat{R}_{ii}(\boldsymbol{k},t)\,d^2\boldsymbol{k}. \tag{2.4}$$

Then, the complex-valued scalar $Z$ is linked to the polarization anisotropy, *i.e.* the difference of energy between components, and is related to the spectral Reynolds tensor through

$$Z(\boldsymbol{k},t) = \frac{1}{2}\hat{R}_{ij}(\boldsymbol{k},t)N_i^*(\boldsymbol{k})N_j^*(\boldsymbol{k}), \tag{2.5}$$

where $N_i$ are helical modes (Cambon & Jacquin 1989; Waleffe 1992) defined as

$$N_j(\boldsymbol{k}) = e_j^{(2)}(\boldsymbol{k}) - ie_j^{(1)}(\boldsymbol{k}), \qquad \boldsymbol{e}^{(1)} = \frac{\boldsymbol{k}\times\boldsymbol{n}}{|\boldsymbol{k}\times\boldsymbol{n}|}, \qquad \boldsymbol{e}^{(2)} = \boldsymbol{e}^{(3)}\times\boldsymbol{e}^{(1)} \qquad \boldsymbol{e}^{(3)} = \boldsymbol{\alpha}, \tag{2.6}$$

where $(\boldsymbol{e}^{(1)}, \boldsymbol{e}^{(2)}, \boldsymbol{e}^{(3)})$ is the Craya-Herring orthonormal right-handed frame of reference associated with a privileged direction $\boldsymbol{n}$. The first step of the derivation proposed by Mons *et al.* (2016) consists in using EDQNM to close the generalized transfer terms in the evolution equations of $\mathcal{E}$ and $Z$, equivalent to (2.2).

The second step starts with the following truncated expansions of the spectral Reynolds stress tensor for $\mathcal{E}$ and $Z$ for moderately anisotropic flows

$$\mathcal{E}(\boldsymbol{k},t) = \mathcal{E}_0\Big(1 - 15H_{ij}^{(dir)}(k,t)\alpha_i\alpha_j\Big), \tag{2.7}$$

$$Z(\boldsymbol{k},t) = \frac{5}{2}\mathcal{E}_0 H_{ij}^{(pol)}(k,t)N_i^*(\boldsymbol{k})N_j^*(\boldsymbol{k}), \tag{2.8}$$

with $\mathcal{E}_0 = E(k,t)/(4\pi k^2)$, and where $H_{ij}^{(dir)}$ and $H_{ij}^{(pol)}$ are deviatoric tensors that describe anisotropy, defined by a spherical integration

$$2E(k,t)H_{ij}^{(dir)}(k,t) = \int_{S_k}\hat{R}_{ij}^{(dir)}(\boldsymbol{k},t)d^2\boldsymbol{k}, \qquad 2E(k,t)H_{ij}^{(pol)}(k,t) = \int_{S_k}\hat{R}_{ij}^{(pol)}(\boldsymbol{k},t)d^2\boldsymbol{k}. \tag{2.9}$$

Finally, these truncated expansions allow to derive evolution equations for the spherically-averaged descriptors $E$, $H_{ij}^{(dir)}$, $H_{ij}^{(pol)}$ (see Table 1). After the spherical integration, the $\boldsymbol{k}$-dependence is transformed into a $k$ one, according to the expansions into spherical harmonics (2.7) and (2.8): these expansions allow to restore a part of the angular dependence information.

### 2.2. *Towards the passive scalar and scalar flux Craya equations*

In order to derive the spectral evolution equations of the scalar-scalar and velocity-scalar second-order correlations, the procedure described in the previous section for obtaining the Craya equation is used. The scalar field $T$ is decomposed into mean and fluctuating parts $T = \Theta + \theta$, with $<\theta>= 0$, and the mean scalar gradient is written

$$\lambda_i = \frac{\partial\Theta}{\partial x_i}, \tag{2.10}$$

so that $\Theta = \lambda_i x_i$. In physical space, the evolution equation of the scalar fluctuation $\theta$ in the homogeneous framework is

$$\frac{\partial\theta}{\partial t} + A_{jl}x_l\frac{\partial\theta}{\partial x_j} + u_j\lambda_j + \frac{\partial}{\partial x_j}(\theta u_j) = a\frac{\partial^2\theta}{\partial x_l\partial x_l}, \tag{2.11}$$

where $a$ is the scalar diffusivity. The Fourier transform of the previous equation yields

$$\left(\frac{\partial}{\partial t} - A_{jl}k_j\frac{\partial}{\partial k_l} + ak^2\right)\hat{\theta} + \lambda_j\hat{u}_j = -ik_j\widehat{\theta u_j}, \tag{2.12}$$

with the convolution product

$$\widehat{\theta u_j}(\boldsymbol{k},t) = \int_{\boldsymbol{k}=\boldsymbol{p}+\boldsymbol{q}}\hat{\theta}(\boldsymbol{p},t)\hat{u}_j(\boldsymbol{q},t)d^3\boldsymbol{p}.$$

Then, the spectral scalar-scalar correlation $\mathcal{E}^T$ is defined as

$$<\hat{\theta}^*(\boldsymbol{p})\hat{\theta}(\boldsymbol{k})>= \mathcal{E}^T(\boldsymbol{k})\delta(\boldsymbol{k}-\boldsymbol{p}), \tag{2.13}$$

which corresponds to the second-order correlation $K_T =< \theta^2 >$ in physical space. $\mathcal{E}^T$ is real and thus satisfies $\mathcal{E}^T(\boldsymbol{k}) = \mathcal{E}^T(-\boldsymbol{k})$ due to Hermitian symmetry. It is linked to the scalar variance spectrum $E_T(k,t)$ through a spherical integral

$$E_T(k,t) = \int_{S_k} \mathcal{E}^T(\boldsymbol{k},t) d^2\boldsymbol{k}. \tag{2.14}$$

The Craya equation for the three-dimensional scalar variance spectrum is then

$$\left(\frac{\partial}{\partial t} - A_{jl}k_j\frac{\partial}{\partial k_l} + 2ak^2\right)\mathcal{E}^T(\boldsymbol{k},t) + 2\lambda_j F_j(\boldsymbol{k},t) = T^{T,NL}(\boldsymbol{k},t). \tag{2.15}$$

$T^{T,NL}$ is the total non-linear scalar transfer which can be written

$$T^{T,NL}(\boldsymbol{k},t) = 2k_i\Re\left(\int S_i^T(\boldsymbol{k},\boldsymbol{p},t)d^3\boldsymbol{p}\right), \tag{2.16}$$

with $\int(...)d^3\boldsymbol{p}$ the integration over the whole spectral domain, and where $S_i^T(\boldsymbol{k},\boldsymbol{p},t)$ is the scalar three-point third-order spectral correlation

$$S_i^T(\boldsymbol{k},\boldsymbol{p},t)\delta(\boldsymbol{k}+\boldsymbol{p}+\boldsymbol{q}) = i < \hat{u}_i(\boldsymbol{q})\hat{\theta}(\boldsymbol{k})\hat{\theta}(\boldsymbol{p}) > . \tag{2.17}$$

The scalar flux $F_i(\boldsymbol{k},t)$, or mixed velocity-scalar correlation, introduced in (2.15) is defined as

$$< \hat{u}_i^*(\boldsymbol{p})\hat{\theta}(\boldsymbol{k}) >= F_i(\boldsymbol{k})\delta(\boldsymbol{k}-\boldsymbol{p}), \tag{2.18}$$

which corresponds to the second-order correlation $R_i^F =< u_i\theta >$ in physical space. The scalar flux Craya equation is then

$$\left(\frac{\partial}{\partial t} - A_{jl}k_j\frac{\partial}{\partial k_l} + (\nu+a)k^2\right)F_i(\boldsymbol{k}) + M_{ij}(\boldsymbol{k})F_j(\boldsymbol{k}) + \lambda_j\hat{R}_{ij}(\boldsymbol{k}) = T_i^{F,NL}(\boldsymbol{k}), \tag{2.19}$$

where $T_F^{T,NL}$ is the non-linear scalar flux transfer which can be written

$$T_i^{F,NL}(\boldsymbol{k},t) = P_{inm}(\boldsymbol{k})\int S_{nm}^F(\boldsymbol{k},\boldsymbol{p},t)d^3\boldsymbol{p} + k_j\int S_{ji}^{F*}(\boldsymbol{p},\boldsymbol{k},t)d^3\boldsymbol{p} \tag{2.20}$$

with $S_{nm}^F(\boldsymbol{k},\boldsymbol{p},t)$ the scalar flux three-point third-order spectral correlation

$$S_{nm}^F(\boldsymbol{k},\boldsymbol{p},t)\delta(\boldsymbol{k}+\boldsymbol{p}+\boldsymbol{q}) = i < \hat{u}_n(\boldsymbol{q})\hat{\theta}(\boldsymbol{k})\hat{u}_m(\boldsymbol{p}) > . \tag{2.21}$$

The form of the non-linear scalar flux transfer (2.20) has been obtained in a recent active scalar study (Burlot *et al.* 2015). Writing $T_i^{F,NL}$ in a manner analogous to the kinetic case (Mons *et al.* 2016) is done by introducing

$$\tau_i^F(\boldsymbol{k},\boldsymbol{p},t) = k_n\int S_{ni}^F(\boldsymbol{k},\boldsymbol{p},t)d^3\boldsymbol{p}, \tag{2.22}$$

so that the non-linear scalar transfer reads

$$T_i^{F,NL}(\boldsymbol{k},t) = \tau_i^F(\boldsymbol{k},\boldsymbol{p},t) + \tau_i^{*F}(\boldsymbol{p},\boldsymbol{k},t) + W_i^F(\boldsymbol{k},t), \tag{2.23}$$

where $W_i^F(\boldsymbol{k},t) = -\alpha_i\alpha_m\tau_m^F(\boldsymbol{k},\boldsymbol{p},t)$ represents non-linear mixed pressure-velocity correlations, from which the RTI of $F_i$ is expected, but not prescribed. This RTI mechanism is responsible for the destruction of the scalar flux since it does not exist in isotropic turbulence. $\tau_i^F + \tau_i^{*F}$ is a conservative transfer quantity with zero-integral over $\boldsymbol{k}$.

### 2.3. *Generalized scalar Lin equations and EDQNM closure*

The generalized Lin equations for the scalar correlation $\mathcal{E}^T$ and the scalar flux $F_i$ can be written

$$\left(\frac{\partial}{\partial t}+2ak^2\right)\mathcal{E}^T(\boldsymbol{k},t)=T^{T,NL}(\boldsymbol{k},t)+T^{T,L}(\boldsymbol{k},t), \tag{2.24}$$

$$\left(\frac{\partial}{\partial t}+(\nu+a)k^2\right)F_i(\boldsymbol{k},t)=T_i^{F,NL}(\boldsymbol{k},t)+T_i^{F,L}(\boldsymbol{k},t). \tag{2.25}$$

$T^{T,L}$ and $T_i^{F,L}$ are the linear passive scalar and scalar flux transfers

$$T^{T,L}(\boldsymbol{k},t)=A_{jl}k_j\frac{\partial\mathcal{E}^T(\boldsymbol{k},t)}{\partial k_l}-2\lambda_l F_l(\boldsymbol{k},t), \tag{2.26}$$

$$T_i^{F,L}(\boldsymbol{k},t)=A_{jl}k_j\frac{\partial F_i(\boldsymbol{k},t)}{\partial k_l}-M_{ij}(\boldsymbol{k})F_j(\boldsymbol{k},t)-\lambda_j\hat{R}_{ij}(\boldsymbol{k},t). \tag{2.27}$$

Now, the non-linear passive scalar and scalar flux transfers $T^{T,NL}$ and $T^{F,NL}$ need to be modelled. The eddy-damped quasi-normal markovian approximation (EDQNM) was first introduced by Orszag (1970); Leith (1971); Orszag (1977) for hydrodynamic turbulence.

Hereafter, an EDQNM closure adapted to homogeneous anisotropic flows is derived similarly to Mons *et al.* (2016). The complete anisotropic form of the second-order spectral tensors is kept in the quasi-normal (QN) formulation, and is therefore expressed in terms of the $\boldsymbol{k}$-vector descriptors of Table 1. Whereas the eddy-damping (ED), which models the contribution from fourth-order cumulants to the equations that govern triple correlations, is kept in an isotropic relationship. Assuming that the scalar probability distributions are close to normal distributions, the QN approximation is used to model the passive scalar and scalar flux non-linear transfers. Then, combining isotropic ED, complete QN, and Markovianisation allows to write from (2.16) and (2.20)

$$T^{T,NL}(\boldsymbol{k},t)=2k_i\int\theta^T_{kpq}\mathfrak{T}_i^{T,QN}(\boldsymbol{k},t)d^3\boldsymbol{p}, \tag{2.28}$$

$$T_i^{F,NL}(\boldsymbol{k},\boldsymbol{p},t)=P_{imn}(\boldsymbol{k})\int\theta^F_{kpq}\mathfrak{T}^F_{nm}(\boldsymbol{k},\boldsymbol{p},t)d^3\boldsymbol{p}+k_j\int\theta^F_{kpq}\mathfrak{T}^{*F}_{ji}(\boldsymbol{p},\boldsymbol{k},t)d^3\boldsymbol{p}. \tag{2.29}$$

$\theta^T_{kpq}$ and $\theta^F_{kpq}$ are the characteristic times of the third-order scalar and scalar flux correlations respectively

$$\theta^T_{kpq}=\frac{1-\exp\left[-(a(k^2+p^2)+\nu q^2+\mu_2(k)+\mu_2(p)+\mu_3(q))t\right]}{a(k^2+p^2)+\nu q^2+\mu_2(k)+\mu_2(p)+\mu_3(q)}, \tag{2.30}$$

$$\theta^F_{kpq}=\frac{1-\exp\left[-(ak^2+\nu(p^2+q^2)+\mu_2(k)+\mu_3(p)+\mu_3(q))t\right]}{ak^2+\nu(p^2+q^2)+\mu_2(k)+\mu_3(p)+\mu_3(q)}. \tag{2.31}$$

$\theta^T_{kpq}$ and $\theta^F_{kpq}$ are obtained by writing the evolution equations of the passive scalar and scalar flux third-order correlations defined in (2.17) and (2.21) respectively. Such an approach for the scalar case has already been used by Bos *et al.* (2005) for homogeneous isotropic turbulence with a scalar gradient (HITSG). The eddy-damping terms $\mu_2$ and $\mu_3$ reflect departure from normal laws and, combined with Markovianization, ensure realizability

$$\mu_2(k,t)=A_2\sqrt{\int_0^k p^2E(p,t)dp},\qquad \mu_3(k,t)=A_3\sqrt{\int_0^k p^2E(p,t)dp},$$

with $A_2=0$ and $A_3=1.3$. The setting of $A_2$ and $A_3$ is discussed in Herring *et al.* (1982);

Lesieur (2008), along with the choice of the eddy-damping terms $\mu_2$ and $\mu_3$. These two constants are set, based on experimental and theoretical considerations, to recover the Corrsin-Obukhov constant $K_{CO} \simeq 0.8$. For the kinetic field, the eddy-damping used in EDQNM is

$$\mu_1(k,t) = A_1 \sqrt{\int_0^k p^2 E(p,t) dp}$$

as defined by Pouquet *et al.* (1975) - as an improved version, more general (assessed in 2D and 3D, at various Reynolds numbers) than in Orszag (1970) - where $A_1 = 0.355$ so that the Kolmogorov constant is recovered $K_0 \simeq 1.3$. As a result of the QN approximation, $\mathfrak{T}_i^{T,QN}$ and $\mathfrak{T}_{ij}^{F,QN}$ can be written

$$\begin{aligned}\mathfrak{T}_i^{T,QN}(\boldsymbol{k},\boldsymbol{p},t) &= 2P_{imn}(\boldsymbol{q})F_n(\boldsymbol{k},t)F_m(\boldsymbol{p},t) + F_i^*(\boldsymbol{q},t)\Big(k_n F_n(\boldsymbol{p},t) + p_n F_n(\boldsymbol{k},t)\Big) \\ &\quad - k_n \hat{R}_{ni}(\boldsymbol{q},t)\Big(\mathcal{E}^T(\boldsymbol{k},t) - \mathcal{E}^T(\boldsymbol{p},t)\Big), \qquad (2.32)\\ \mathfrak{T}_{ij}^{F,QN}(\boldsymbol{k},\boldsymbol{p},t) &= k_n\Big(\hat{R}_{ni}(\boldsymbol{q},t)F_j^*(\boldsymbol{p},t) + \hat{R}_{nj}(\boldsymbol{p},t)F_i^*(\boldsymbol{q},t)\Big) \\ &\quad + 2F_m(\boldsymbol{k},t)\Big(P_{imn}(\boldsymbol{q})\hat{R}_{nj}(\boldsymbol{p},t) + P_{jmn}(\boldsymbol{p})\hat{R}_{ni}(\boldsymbol{q},t)\Big). \qquad (2.33)\end{aligned}$$

With this closure, and with calculations very similar to the kinetic case, the non-linear scalar transfer becomes

$$\begin{aligned}T^{T,NL}(\boldsymbol{k},t) &= 2\int \theta_{kpq}^T kp(xy+z)(\mathcal{E}'' + \Re X'')(\mathcal{E}'^T - \mathcal{E}^T)d^3\boldsymbol{p} \\ &\quad + 2\int \theta_{kpq}^T\Big(k_n F_n'^*(p_m F_m + k_m F_m') + p_m F_m k_n F_n' \frac{ky - px}{q}\Big)d^3\boldsymbol{p}. \qquad (2.34)\end{aligned}$$

The symbols $'$ and $''$ refer to wave vectors $\boldsymbol{p}$ and $\boldsymbol{q}$ respectively. $x$, $y$ and $z$ are cosines of the angles formed by the triad vectors $(\boldsymbol{k},\boldsymbol{p},\boldsymbol{q})$. $X = Ze^{2i\lambda}$, $X' = Z'e^{2i\lambda'}$ and $X'' = Z''e^{2i\lambda''}$, where $\lambda$, $\lambda'$ and $\lambda''$ are rotation angles of the triad around $\boldsymbol{k}$, $\boldsymbol{p}$ and $\boldsymbol{q}$ respectively, and $Z$ has been defined in (2.5). Since the scalar flux exists only in an anisotropic configuration, and is thus a purely anisotropic field, the second part of (2.34) is neglected for moderately anisotropic flows, where all quadratic anisotropic contributions can be neglected. The closure for $F_i(\boldsymbol{k})$ is developed with an appropriate decomposition in the following section.

## 3. Spherically-averaged scalar Lin equations

This section presents the final step of the modelling. Spherically-averaged evolution equations for the scalar variance spectrum, the scalar directivity and the scalar flux are derived from the previous generalized scalar Lin equations (2.24) and (2.25). These final scalar equations depend only on the modulus $k$ of the wave vector $\boldsymbol{k}$.

### 3.1. *Spherically-averaged descriptors*

A decomposition similar to the one of $\mathcal{E}$ in the kinetic case is used for the scalar correlation

$$\mathcal{E}^T(\boldsymbol{k},t) = \frac{E_T(k,t)}{4\pi k^2}\Big(1 - 15H_{ij}^{(T)}(k,t)\alpha_i\alpha_j\Big) = \mathcal{E}_0^T(\boldsymbol{k},t) + \mathcal{E}^{(T,dir)}(\boldsymbol{k},t), \qquad (3.1)$$

with $\mathcal{E}^{(T,dir)} = -15\mathcal{E}_0^T H_{ij}^{(T)}\alpha_i\alpha_j$ and $\mathcal{E}_0^T = E_T/(4\pi k^2)$. The following decomposition is chosen for the scalar flux

$$F_i(\boldsymbol{k},t) = \frac{3}{2}\,\mathcal{E}_j^F(k,t)\,P_{ij}(\boldsymbol{k}). \qquad (3.2)$$

| | Spherically averaged descriptors | | |
|---|---|---|---|
| $\boldsymbol{k}$-vectors descriptors | Isotropy | Directional anisotropy | Polarization anisotropy |
| $\mathcal{E}(\boldsymbol{k},t)$ | $E(k,t)$ | $H_{ij}^{(dir)}(k,t)$ | 0 |
| $Z(\boldsymbol{k},t)$ | 0 | 0 | $H_{ij}^{(pol)}(k,t)$ |
| $\mathcal{E}^T(\boldsymbol{k},t)$ | $E_T(k,t)$ | $H_{ij}^{(T)}(k,t)$ | 0 |
| $F_i(\boldsymbol{k},t)$ | 0 | 0 | $E_i^F(k,t)$ |

TABLE 1. Description of anisotropy at the velocity, passive scalar and scalar flux levels, using $\boldsymbol{k}$-vectors descriptors and their corresponding spherically-averaged contributions. $\mathcal{E}$, $Z$, $\mathcal{E}^T$ and $F_i$ are defined respectively in (2.4), (2.5), (2.13) and (2.18).

This decomposition is consistent with the scalar flux being a solenoidal field ($k_i F_i = 0$). These equations (3.1) and (3.2) are exact in HITSG (Herr *et al.* 1996). Whereas they are truncations at the first non-trivial order (the second order) of the scalar correlation $\mathcal{E}^T$ and scalar flux $F_i$ expansions for the cases involving mean velocity gradients (HST and HSTSG). These truncations are consistent with the modelling of $\mathcal{E}$ and $Z$ done in (2.7) and (2.8) respectively.

Hermitian symmetry for the scalar flux, $F_i(-\boldsymbol{k}) = F_i^*(\boldsymbol{k})$, is straightforward from the decomposition of a vector into helical modes. Notably, it implies that the vector $\mathcal{E}_j^F$ is purely real. About the distinction between directional and polarization anisotropies: scalars admit directional anisotropy only. Consequently, $H_{ij}^{(T)}$, which appears in the expansion of $\mathcal{E}^T$, reflects directional anisotropy, as $H_{ij}^{(dir)}$ in the decomposition of $\mathcal{E}$. Then, as $F_i$ is a vector, $\mathcal{E}_j^F$ represents polarization anisotropy. Finally, a solenoidal second-order tensor such as $\hat{R}_{ij}$ admits both contributions (Cambon & Rubinstein 2006). This classification is summarized in Table 1.

An additional solenoidal contribution in terms of the Levi-Civita permutation tensor is discussed by O'Gorman & Pullin (2005), resulting in the so-called *quadrature spectrum*. It can be shown that using a toroidal-poloidal decomposition of a solenoidal vector, the latter contribution is redundant with the projection part in (3.2). Therefore, as the helicity spectrum (Gomez *et al.* 2000) is neglected in the spectral Reynolds stress tensor, this additional solenoidal contribution is consistently discarded.

The scalar anisotropic descriptor $H_{ij}^{(T)}$ and the spherically-averaged scalar flux $E_i^F$ are defined similarly to the kinetic ones $H_{ij}^{(dir)}$ and $H_{ij}^{(pol)}$ using spherical integration

$$2E_T(k,t)H_{ij}^{(T)}(k,t) = \int_{S_k} \mathcal{E}^{(T,dir)}(\boldsymbol{k},t)P_{ij}d^2\boldsymbol{k}, \tag{3.3}$$

$$E_i^F(k,t) = \int_{S_k} F_i(\boldsymbol{k},t)d^2\boldsymbol{k}. \tag{3.4}$$

The scalar anisotropy tensor $b_{ij}^T$ is then given by

$$b_{ij}^T(t) = \frac{1}{K_T(t)} \int_0^\infty E_T(k,t)H_{ij}^{(T)}(k,t)dk, \tag{3.5}$$

and is analogous in the description of anisotropy to $b_{ij}^{(dir)}$ for the velocity field (Mons *et al.* 2016). Similar scalar anisotropy descriptors were introduced by Kassinos *et al.* (2007), with a slightly different convention for structure-based modelling. Finally, the scalar

energy $K_T$, or scalar variance, and its dissipation rate are defined as

$$K_T(t) =< \theta^2 >= \int_0^\infty E_T(k,t)dk, \qquad \epsilon_T(t) = 2a\int_0^\infty k^2 E_T(k,t)dk. \tag{3.6}$$

### 3.2. *Spherical average of the passive scalar and scalar flux fields*

The final evolution equations for the spherically-averaged scalar descriptors, derived from the previous generalized Lin equations, and briefly called spherically-averaged scalar Lin equations, read

$$\left(\frac{\partial}{\partial t} + 2ak^2\right) E_T(k,t) = S^{T,NL(iso)}(k,t) + S^{T,L(iso)}(k,t), \tag{3.7}$$

$$\left(\frac{\partial}{\partial t} + 2ak^2\right) E_T(k,t)H_{ij}^{(T)}(k,t) = S_{ij}^{T,NL(dir)}(k,t) + S_{ij}^{T,L(dir)}(k,t), \tag{3.8}$$

$$\left(\frac{\partial}{\partial t} + (a+\nu)k^2\right) E_i^F(k,t) = S_i^{F,NL}(k,t) + S_i^{F,L}(k,t). \tag{3.9}$$

$S^{T,NL(iso)}$ is the classical non-linear spherically-averaged isotropic scalar transfer

$$\begin{aligned} S^{T,NL(iso)}(k,t) &= \int_{S_k} T^{T,NL}(\boldsymbol{k},t)d^2\boldsymbol{k} \\ &= \int_{\Delta_k} 16\theta_{kpq}^T \pi^2 k^2 p^2 q(xy+z)\mathcal{E}_0''(\mathcal{E}_0'^T - \mathcal{E}_0^T)dpdq, \end{aligned} \tag{3.10}$$

which is exactly the one derived by Lesieur (2008). $S_{ij}^{T,NL(dir)}$ is the non-linear spherically-averaged directional scalar transfer

$$\begin{aligned} S_{ij}^{T,NL(dir)}(k,t) &= \frac{1}{2}\int_{S_k} T^{T,NL}P_{ij}(\boldsymbol{k},t)d^2\boldsymbol{k} - \frac{\delta_{ij}}{3}S^{T,NL(iso)}(k,t) \\ &= \int_{\Delta_k} 4\pi^2\theta_{kpq}^T k^2p^2q(xy+z)(y^2-1)\mathcal{E}_0''(\mathcal{E}_0'^T - \mathcal{E}_0^T)H_{ij}''^{(pol)}dpdq \\ &+ \int_{\Delta_k} 8\pi^2\theta_{kpq}^T k^2p^2q(xy+z)(3y^2-1)\mathcal{E}_0''(\mathcal{E}_0'^T - \mathcal{E}_0^T)H_{ij}''^{(dir)}dpdq \\ &+ \int_{\Delta_k} 8\pi^2\theta_{kpq}^T k^2p^2q(xy+z)\mathcal{E}_0''\Big((3z^2-1)\mathcal{E}_0'^T H_{ij}'^{(T)} - 2\mathcal{E}_0^T H_{ij}^{(T)}\Big)dpdq \end{aligned} \tag{3.11}$$

with $\Delta_k$ the domain where $k$, $p$ and $q$ are modulus of the triad vectors. $S^{T,NL(iso)}$ is a conservative transfer, meaning that its integral over $k$ is zero. However, the integral of $S_{ij}^{T,NL(dir)}$ is different from zero (like the directional transfer of the velocity field). From the non-conservative part of $S_{ij}^{T,NL(dir)}$, a return to isotropy of the passive scalar is expected. Nevertheless, as there is no fluctuating pressure in the passive scalar equation, it cannot return to isotropy on its own, and therefore, this mechanism is driven by the dynamics of the velocity field only. For the linear terms, $S^{T,L(iso)}$ is the linear spherically-averaged isotropic scalar transfer

$$S^{T,L(iso)}(k,t) = \int_{S_k} T^{T,L}(\boldsymbol{k},t)d^2\boldsymbol{k} = -2A_{ln}^+\frac{\partial}{\partial k}(kE_T H_{ln}^{(T)}) - 2\lambda_l E_l^F. \tag{3.12}$$

$S_{ij}^{T,L(dir)}$ is the linear spherically-averaged directional scalar transfer

$$\begin{aligned}
S_{ij}^{T,L(dir)}(k,t) &= \frac{1}{2}\int_{S_k} T^{T,L}(\boldsymbol{k},t)P_{ij}d^2\boldsymbol{k} - \frac{\delta_{ij}}{3}S^{T,L(iso)}(k,t)\\
&= -\frac{3}{7}E_T\Big(A_{lj}^+H_{il}^{(T)} + A_{li}^+H_{jl}^{(T)} - \frac{2}{3}A_{ln}^+\delta_{ij}H_{ln}^{(T)}\Big) + \frac{1}{5}A_{ij}^+E_T\\
&+ \frac{2}{7}\left(A_{il}^+\frac{\partial}{\partial k}(kE_TH_{jl}^{(T)}) + A_{jl}^+\frac{\partial}{\partial k}(kE_TH_{il}^{(T)}) - \frac{2}{3}A_{lm}^+\delta_{ij}\frac{\partial}{\partial k}(kE_TH_{lm}^{(T)})\right)\\
&- \frac{1}{15}A_{ij}^+\frac{\partial}{\partial k}(kE_T) - E_T\Big(A_{lj}^-H_{il}^{(T)} + A_{li}^-H_{jl}^{(T)}\Big)\\
&- \frac{1}{10}\Big(\lambda_iE_j^F + \lambda_jE_i^F - \frac{2}{3}\lambda_lE_l^F\delta_{ij}\Big),
\end{aligned} \tag{3.13}$$

where $A_{ij}^+$ and $A_{ij}^-$ respectively denote the symmetric and antisymmetric parts of the velocity mean-gradient matrix. $\lambda_i$ is the mean scalar gradient and $E_i^F = 4\pi k^2\,\mathcal{E}_i^F$.

Regarding the scalar flux, its non-linear transfer becomes, at first order in anisotropy,

$$\begin{aligned}
T_i^{F,NL}(\boldsymbol{k},t) &= \frac{3}{2}\int\theta_{kpq}^F k\mathcal{E}_0'\Bigg[\mathcal{E}_j^F\Bigg(2px(\alpha_i + z\alpha_i')(\alpha_j'' + y\alpha_j)\\
&+ q(y+xz)\Big(2\alpha_i''(\alpha_j'' + y\alpha_j) - P_{ij}\Big)\Bigg) + k\mathcal{E}_j^{F''}\Bigg((1-z^2)P_{ij}'' + (\alpha_i + z\alpha_i')(\alpha_j + y\alpha_j'')\Bigg)\Bigg]d^3\boldsymbol{p}\\
&+ \frac{3}{2}\int\theta_{pkq}^F k\Bigg[q\mathcal{E}_0\mathcal{E}_j^{F'}(\alpha_i'' + y\alpha_i)\Big(\alpha_j + z\alpha_j' + 2y(\alpha_j'' + x\alpha_j')\Big)\\
&+ k\mathcal{E}_0''\mathcal{E}_j^{F'}\Bigg((\alpha_i + y\alpha_i'')(\alpha_j + z\alpha_j') + (1-y^2)\Big(P_{ij}' - 2\alpha_i(\alpha_j + z\alpha_j')\Big)\Bigg)\\
&+ p\Bigg(\mathcal{E}_0\mathcal{E}_j^{F''}(\alpha_i' + z\alpha_i)(\alpha_j + y\alpha_j'') - (xy+z)\mathcal{E}_0''\mathcal{E}_j^F P_{ij}\Bigg)\Bigg]d^3\boldsymbol{p}\\
&- 3\int\theta_{kpq}^F k\alpha_i\Bigg[k(1-y^2)\mathcal{E}_0''\mathcal{E}_j^{F'}(\alpha_j + z\alpha_j') + q\mathcal{E}_0'\mathcal{E}_j^F(1 - z^2 - 2y(y+xz))(\alpha_j'' + y\alpha_j)\Bigg]d^3\boldsymbol{p}.
\end{aligned} \tag{3.14}$$

One can observe that in the framework of moderate anisotropy, only the isotropic part of the velocity field $\mathcal{E}_0 = E/(4\pi k^2)$ remains. The non-linear spherically-averaged scalar flux transfer is then

$$\begin{aligned}
S_i^{F,NL}(k,t) &= \int_{S_k} T_i^{F,NL}(\boldsymbol{k},t)d^2\boldsymbol{k}\\
&= 4\pi^2\int_{\Delta_k}\theta_{kpq}^F k^2pq\mathcal{E}_0'\Bigg[k\mathcal{E}_i^{F''}(1 + y^2 - z^2 - xyz - 2y^2z^2) - 2q(y^3 + xz)\mathcal{E}_i^F\Bigg]dpdq\\
&+ 4\pi^2\int_{\Delta_k}\theta_{pkq}^F k^2pq\Bigg[\mathcal{E}_0\Bigg(qz(2xy^2 + yz - x)\mathcal{E}_i^{F'} - py(x+yz)\mathcal{E}_i^{F''}\Bigg)\\
&+ k\mathcal{E}_0''\Bigg((1 - y^2 + z^2 - xyz - 2y^2z^2)\mathcal{E}_i^{F'} - 2(1-y^2)\mathcal{E}_i^F\Bigg)\Bigg]dpdq.
\end{aligned} \tag{3.15}$$

One can extract from this non-linear scalar-flux transfer the mixed pressure-velocity part,

which is expected to have a RTI function

$$S_i^{F,RTI}(k,t) = -8\int_{\Delta_k} \pi^2 \theta^F_{kpq} k^3 pq \mathcal{E}'_0 \mathcal{E}_i^{F''}(1-y^2)(1-z^2)dpdq. \tag{3.16}$$

And $S_i^{F,L}$ is the spherically-averaged linear scalar flux transfer

$$\begin{aligned} S_i^{F,L}(k,t) &= \int_{S_k} T_i^{F,L}(\boldsymbol{k},t)d^2\boldsymbol{k} \\ &= -2\lambda_j E\Big(\frac{1}{3}\delta_{ij} + H_{ij}^{(dir)} + H_{ij}^{(pol)}\Big) - \frac{1}{5}A_{ij}^{+}\Big(2E_j^F + \frac{\partial}{\partial k}(kE_j^F)\Big). \end{aligned} \tag{3.17}$$

As a conclusion, the dynamics of a passive scalar field in homogeneous anisotropic turbulence is driven by six spherically-averaged compact equations within this anisotropic EDQNM modelling: three for the velocity field first given in Mons *et al.* (2016)

$$\left(\frac{\partial}{\partial t} + 2\nu k^2\right) E(k,t) = S^{NL(iso)}(k,t) + S^{L(iso)}(k,t), \tag{3.18}$$

$$\left(\frac{\partial}{\partial t} + 2\nu k^2\right) E(k,t) H_{ij}^{(dir)}(k,t) = S_{ij}^{NL(dir)}(k,t) + S_{ij}^{L(dir)}(k,t), \tag{3.19}$$

$$\left(\frac{\partial}{\partial t} + 2\nu k^2\right) E(k,t) H_{ij}^{(pol)}(k,t) = S_{ij}^{NL(pol)}(k,t) + S_{ij}^{L(pol)}(k,t), \tag{3.20}$$

two for the passive scalar ((3.7) and (3.8)), and one for the scalar flux (3.9). The last three ones are original results of the present work. The different anisotropy descriptors are gathered in Table 1.

### 3.3. *Numerical parameters, initial conditions, validity of the model*

The time evolution of the kinetic spectra $\left(E, EH_{ij}^{(dir)}, EH_{ij}^{(pol)}\right)$ and the passive scalar and scalar flux spectra $\left(E_T, E_T H_{ij}^{(T)}, E_i^F\right)$ are obtained by solving 20 coupled integro-differential equations using a third order Runge-Kutta scheme with implicit treatment of diffusion terms. The wavenumber space is discretized using a logarithmic mesh $k_{i+1} = 10^{1/f}k_i$ for $1 \leqslant i \leqslant n$, where $n$ is the number of modes and $f = 17$ the number of discrete points per decade. This mesh spans from $k_{\min}$ to $k_{\max} = 10k_\eta$ where $k_\eta = (\epsilon/\nu^3)^{1/4}$ is the Kolmogorov wavenumber. Such a resolution at high Reynolds numbers allows a fine description of the viscous range, with a $k_{\min}$ higher than the ones usually used in DNS. The time step is monitored by defining a constant $CFL$ number and is obtained by considering the characteristic time scales of scalar and kinetic dynamics. The values of the physical and numerical parameters are given for simulations at large and small Reynolds number in Table 2. If not mentioned otherwise, the initial conditions are isotropic ($F_i(k,t=0) = 0$) with the kinetic energy spectrum $E(k,t=0)$ proposed by Pope (2000); Meyers & Meneveau (2008)

$$E(k,t=0) = K_0\, k^{-5/3}\, \epsilon^{2/3} f_L(kL)\, f_\eta(k\eta), \tag{3.21}$$

where $f_L$ and $f_\eta$ are shape functions for large and small scales respectively

$$f_L(x) = \left(\frac{x}{(x^{1.5} + 1.5 - \sigma/4)^{2/3}}\right)^{\frac{5}{3}+\sigma}, f_\eta(x) = \exp\Big(-5.3((x^4 + 0.4^4)^{\frac{1}{4}} - 0.4)\Big), \tag{3.22}$$

where $\sigma$ is the infrared slope. Simulations have shown that initial conditions moderately anisotropic only slightly impact the early dynamics, without altering the asymptotic

| Kind of anisotropy | $Re_\lambda(t=0)$ | $Pr$ | CFL | $k_{\min}$ | $k_{\max}$ |
|---|---|---|---|---|---|
| HITSG | $10^4$ | 1 | 0.3 | $10^{-7}k_L(t=0)$ | $10k_\eta$ |
| HITSG towards low Reynolds | $10^4$ | 1 | 0.3 | $10^{-16}k_L(t=0)$ | $10k_\eta$ |
| HST | 1 | 1 | 0.3 | $10^{-10}k_L(t=0)$ | $10^5k_\eta$ |
| HSTSG | 1 | 1 | 0.3 | $10^{-10}k_L(t=0)$ | $10^5k_\eta$ |

TABLE 2. Physical and numerical parameters used for the simulations. $k_L$ and $k_\eta$ are the integral and Kolmogorov wavenumbers respectively. The initial value of the Reynolds number $Re_\lambda = K\sqrt{20/3\nu\epsilon}$ can be different when it comes to comparisons with experiments and DNS, along with the Prandtl number, often set to 0.7.

states. Thus, classical isotropic initial conditions are used such as $E_T(k,0) = E(k,0)$, avoiding the introduction of supplementary numerical parameters.

In what follows, the Prandtl number is equal to one, meaning that $a = \nu$, and integrated quantities correspond to quantities obtained by integration over the whole wavenumber space, such as the kinetic energy.

It has been mentioned several times that the present model is valid for moderate anisotropy as quadratic contributions in terms of anisotropy descriptors have been neglected. In this view, criteria need to be given to quantify the upper bounds of the anisotropy that the model can handle at the levels of the velocity and scalar fields. Such criteria, or realizability conditions, can be derived directly come from (2.7) and (3.1), to ensure that the kinetic and scalar energy densities $\mathcal{E}$ and $\mathcal{E}^T$ are positive. This yields

$$\max_{i=1,2,3}(\mathcal{L}_i) \leqslant \frac{1}{15}, \qquad \max_{i=1,2,3}(\mathcal{L}_i^T) \leqslant \frac{1}{15}, \tag{3.23}$$

where $\mathcal{L}_i$ and $\mathcal{L}_i^T$ are eigenvalues of $H_{ij}^{(dir)}$ and $H_{ij}^{(T)}$ respectively. In the following simulations, these realizability conditions are a posteriori systematically verified as satisfied. Moreover, it is worth noting that the violation of (3.23) immediately yields negative values for the spectra $E(k,t)$ and $E_T(k,t)$. Hence, moderate anisotropy could be roughly defined as the case for which the intensity of the mean-fields gradients is such that the realizability conditions are satisfied.

## 4. Comparisons with experiments and DNS

In the two previous sections, spherically-averaged evolution equations were derived to investigate the dynamics of a passive scalar and its flux in homogeneous anisotropic turbulence. The modelling of anisotropy within the complete EDQNM approach, labelled as EDQNM in what follows, is now assessed by comparisons to several DNS and experiments at moderate Reynolds numbers in the three configurations presented in the introduction: HITSG, HST and HSTSG. In each case, definitions and basic results are recalled. In what follows, the infrared range refers to very large scales, and from this point, large scales kinetic and scalar infrared slopes are the same, *i.e.* $\sigma = \sigma_T$. This is justified in the Appendix A, and these infrared slopes are defined as $E(k < k_L, t) \sim k^\sigma$ and $E_T(k < k_T, t) \sim k^{\sigma_T}$, with $k_L$ and $k_T$ the integral kinetic and scalar wavenumbers respectively.

### 4.1. *Homogeneous isotropic turbulence with a mean scalar gradient (HITSG)*

In this section, the emphasis is put on the specific case where the scalar flux appears due to an uniform mean gradient $\lambda_j = (0, 0, -\Lambda)$ with $\Lambda > 0$, whereas the velocity field is

purely isotropic and decreases with time. This configuration has been widely investigated (Bos *et al.* 2005; O'Gorman & Pullin 2005; Bos 2014): turbulent eddies bring the hot fluid to the cold parts of the flow (and the opposite) thus creating a turbulent flux.

4.1.1. *Definitions and spectral behaviour*

Firstly, some definitions are given. When the kinetic field is isotropic, it tends to destroy the scalar flux $F_i$, whose dynamics is given by (3.4) and (3.9), created by the scalar gradient $\Lambda$. Given the form of the production transfer term $S_i^{F,L}$, only the third component of $E_i^F$ is non-zero, and its sign is opposite to the one of $\Lambda$. Hence, the cospectrum is defined by

$$\mathcal{F}(k,t) = E_3^F(k,t). \tag{4.1}$$

The cospectrum energy and cospectrum dissipation rate are straightforwardly

$$K_{\mathcal{F}}(t) = \int_0^\infty \mathcal{F}(k,t)dk, \qquad \epsilon_{\mathcal{F}}(t) = (\nu + a)\int_0^\infty k^2\mathcal{F}(k,t)dk. \tag{4.2}$$

Finally, in homogeneous turbulence, the time evolution of the velocity-scalar correlation $R_i^F(t) =< u_i\,\theta >$ is

$$\frac{dR_i^F}{dt} + R_{ij}\lambda_j + A_{ij}R_j^F =< p\frac{\partial\theta}{\partial x_i} > -\epsilon_i^F, \tag{4.3}$$

with $A_{ij} = 0$ in HITSG, and

$$\epsilon_i^F(t) = (\nu + a) < \frac{\partial u_i}{\partial x_l}\frac{\partial\theta}{\partial x_l} >, \qquad \epsilon_{\mathcal{F}} = \epsilon_3^F. \tag{4.4}$$

In the case of a simple scalar gradient ($R_3^F = K_{\mathcal{F}}$), the previous evolution equation simplifies into

$$\frac{dK_{\mathcal{F}}}{dt}(t) = P_{\mathcal{F}}(t) - \epsilon_{\mathcal{F}}(t) + \Pi_{\mathcal{F}}(t), \tag{4.5}$$

where

$$\Pi_{\mathcal{F}}(t) = \int_0^\infty S_3^{F,NL}(k,t)dk \tag{4.6}$$

is the cospectrum destruction, or cospectrum pseudo return to isotropy, driven by the fluctuating pressure of the kinetic field. $P_{\mathcal{F}}$ is the cospectrum production

$$P_{\mathcal{F}}(t) = \int_0^\infty S_3^{F,L}(k,t)dk = \frac{2}{3}\Lambda K(t). \tag{4.7}$$

In homogeneous isotropic turbulence with a scalar gradient (HITSG), the cospectrum is initially zero. The spectral scaling of the cospectrum can be deduced by dimensional analysis, as proposed by Lumley (1967), Bos *et al.* (2005) and O'Gorman & Pullin (2005). One has to assume that $\mathcal{F}$ only depends on the scalar gradient $\Lambda$, the wavenumber $k$ and the kinetic energy dissipation rate $\epsilon$ so that

$$\mathcal{F}(k,t) = C_{\mathcal{F}}\Lambda\epsilon^{1/3}k^{-7/3}, \tag{4.8}$$

where $C_{\mathcal{F}}$ is the cospectrum constant, found to be $C_{\mathcal{F}} \simeq 3$ in the present work. Bos *et al.* (2005) reported $C_{\mathcal{F}} \simeq 1.5$ whereas O'Gorman & Pullin (2005) computed $C_{\mathcal{F}} = 3.5$ with their asymptotic high Reynolds numbers model. The $k^{-7/3}$ scaling is similar to the velocity cross-component spectral tensor in shear turbulence (Lumley 1967). If one assumes that $\mathcal{F}$ depends on $\epsilon$, $k$ and its dissipation rate $\epsilon_{\mathcal{F}}$, then $\mathcal{F} \sim \epsilon^{-1/3}\epsilon_{\mathcal{F}}k^{-5/3}$, which is similar to a passive scalar variance spectrum scaling. This approach would imply that

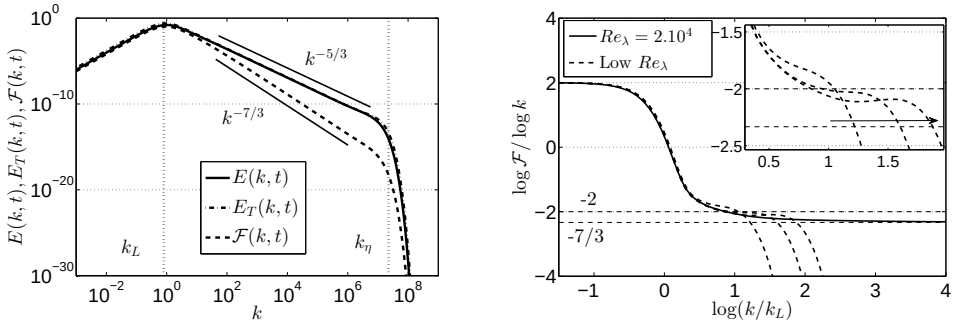


FIGURE 1. At left, cospectrum, kinetic energy and scalar spectra $\mathcal{F}$, $E$ and $E_T$ for $Re_\lambda = 2.10^5$, as a function of the wavenumber $k$, along with the integral and Kolmogorov wavenumbers $k_L$ and $k_\eta$. At right, effects of low Reynolds numbers on the scaling of $\mathcal{F}$, obtained with $\log \mathcal{F}/\log k$, as a function of $\log k/k_L$, with a zoom on the narrow inertial range for the low $Re_\lambda$ curves $Re_\lambda = 50$, $Re_\lambda = 100$, $Re_\lambda = 150$: the arrow indicates the sense of increasing Reynolds numbers. Both for Saffman turbulence ($\sigma = 2$).

the cospectrum dissipation rate $\epsilon_{\mathcal{F}}$ is conserved throughout the cascade and this cannot be satisfied due to the pressure effects (Bos *et al.* 2004).

In what follows, for numerical simulations, one needs to define a dimensionless mean scalar gradient $\mathcal{S}_\theta$. There are different possibilities to define a reference mean scalar gradient $\Lambda_{\text{ref}}$, unlike the mean velocity gradient which is unambiguously defined (De Souza *et al.* 1995). The dimensionless mean scalar gradient is defined as

$$\mathcal{S}_\theta = \frac{\Lambda}{\Lambda_{\text{ref}}}. \tag{4.9}$$

The reference mean scalar gradient $\Lambda_{\text{ref}}$ is defined explicitly in the following comparisons. If not mentioned otherwise, $\mathcal{S}_\theta = 1$ is chosen.

In figure 1, the $k^{-7/3}$ scaling clearly appears for the cospectrum. However, as previously reported by Bos *et al.* (2005), it requires a high Reynolds number ($Re_\lambda \geqslant 10^4$ here). This condition is very important. Indeed, without it, there is no clear power law, neither $k^{-7/3}$ nor $k^{-2}$, as revealed in figure 1 for the three moderate Reynolds number cases $50 \leqslant Re_\lambda \leqslant 150$. The inertial range is rather narrow, and there is a transitory slope which tends to $-7/3$ as $Re_\lambda$ increases. Hence, the $k^{-2}$ scaling reported in previous works seems to be a low Reynolds number effect, that occurs around $Re_\lambda = 100$, typical for DNS. The $k^{-7/3}$ scaling has also been obtained experimentally (Mydlarski 2003), in DNS (O'Gorman & Pullin 2005; Watanabe & Gotoh 2007) or with classical EDQNM (Bos *et al.* 2005; Bos & Bertoglio 2007).

An interesting point to mention, that has not been explicitly reported so far, is about the infrared range of the cospectrum. Indeed, as $\mathcal{F} = 0$ in the initial isotropic flow, one can wonder how it evolves at very large scales. The result is displayed in figure 2: the cospectrum infrared exponent is the same as the kinetic one $\sigma$. This is of importance for the results presented in §5. Moreover, the $k^{-7/3}$ scaling is recovered for all the $\sigma$ presented. Finally, the linear and non-linear transfers associated to the cospectrum are presented in figure 2: $S_3^{F,NL} - S_3^{F,RTI}$ represents the conservative non-linear transfer with zero integral over $k$. $S_3^{F,RTI}$ is the return to isotropy transfer associated with pressure effects. $S_3^{F,NL}$ is the total non-linear transfer that corresponds to a non-conservative flux because of the RTI mechanism. And $S_3^{F,L}$ is the linear transfer responsible for production of anisotropy through the scalar gradient, which decreases with time as the kinetic spectrum $E(k,t)$.

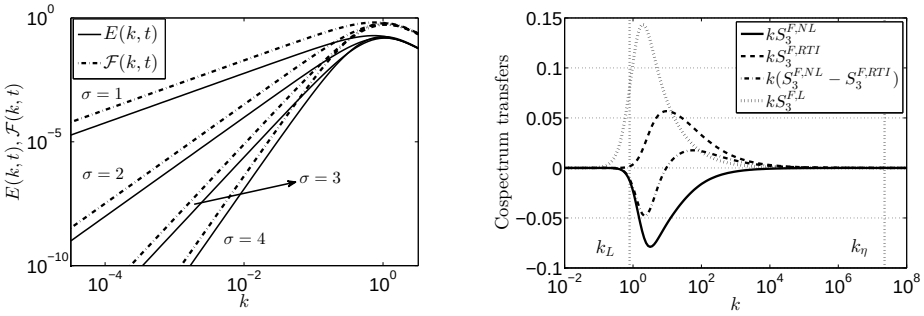


FIGURE 2. At left, large scales spectral scaling of the cospectrum $\mathcal{F}$ for different kinetic infrared slopes $\sigma$ after several turn-over times, as a function of the wavenumber $k$. At right, linear and non-linear transfers of the cospectrum for $\sigma = 2$ at $Re_\lambda = 2.10^5$ as a function of the wavenumber $k$.

4.1.2. *Comparison with Overholt & Pope (1996)*

The focus is put on the ratio of the cospectrum dissipation $\epsilon_\mathcal{F}$ and cospectrum production $P_\mathcal{F}$. In the DNS of Overholt & Pope (1996), it is shown that the cospectrum dissipation is not negligible at low Reynolds number even though it decreases with $Re_\lambda$. The following power law is found

$$\left(\frac{\epsilon_\mathcal{F}}{P_\mathcal{F}}\right)^{\text{DNS}} = 4.61 Re_\lambda^{-0.769}$$

for four different DNS from $Re_\lambda = 28$ to 185, reported in figure 3 along with results coming from the present anisotropic EDQNM simulations for comparison purposes

$$\left(\frac{\epsilon_\mathcal{F}}{P_\mathcal{F}}\right)^{\text{EDQNM}} = 11.6 Re_\lambda^{-0.760}.$$

In the present case, this ratio is evaluated for Reynolds numbers such that the kinetic field decreases according to CBC theory (Comte-Bellot & Corrsin 1966). The satisfactory agreement with DNS regarding the $Re_\lambda$ power law for low Reynolds numbers partially validates the model for the cospectrum. The discrepancy for the numerical factor may arise from the fact that in the DNS the velocity field is forced, whereas it is freely decaying here. The interesting result is that the $Re_\lambda$ power law is valid in both decaying and forced turbulence, and does not depend on the infrared slope $\sigma$. As for the high Reynolds numbers regime, the $Re_\lambda^{-1}$ predicted by Bos *et al.* (2005) is recovered numerically in figure 3 as well. This scaling law can be obtained analytically by direct computation, assuming that for high Reynolds numbers, the dominant region of the kinetic spectrum and cospectrum is the inertial range

$$\frac{\epsilon_\mathcal{F}(t)}{P_\mathcal{F}(t)} = \frac{3(\nu+a)}{2\Lambda} \frac{\int_0^\infty k^2 \mathcal{F}(k,t) dk}{\int_0^\infty E(k,t) dk} \sim \frac{\epsilon^{1/3} \int_{k_L}^{k_\eta} k^{-1/3} dk}{\epsilon^{2/3} \int_{k_L}^{k_\eta} k^{-5/3} dk}.$$

Then, using classical relations such as $(k_\eta/k_L) = Re_L^{3/4}$ where $Re_L$ is the integral Reynolds number so that $\sqrt{20 Re_L/3} = Re_\lambda$, and $\nu k_\eta^{4/3} = \epsilon^{1/3}$, one finds $\epsilon_\mathcal{F}/P_\mathcal{F} \sim Re_\lambda^{-1}$.

4.1.3. *Comparison with Sirivat & Warhaft (1983)*

In this part, results provided by the present model are compared with the experimental work of Sirivat & Warhaft (1983) in the HITSG configuration. The case where the scalar

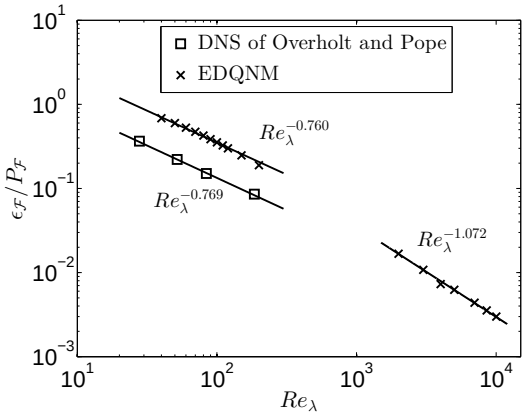


FIGURE 3. Comparison with the DNS by Overholt & Pope (1996) of the ratio of cospectrum dissipation $\epsilon_\mathcal{F}$ and production $P_\mathcal{F}$, both defined in (4.4) and (4.7), for high and low Reynolds numbers, as a function of the Reynolds number $Re_\lambda$. Simulations for $\sigma = 2$ and $\mathcal{S}_\theta = 1$. $\times$ and $\square$ represent respectively EDQNM simulations and DNS. Lines are best-fit power laws.

gradient is created with a mandoline (a screen of thin heated wires) is considered. The parameters of the experiment are the following ones: the input velocity is $U = 3.4m.s^{-1}$ and the meshsize $M = 0.024m$. For this configuration, the initial Reynolds is $Re_\lambda(0) = 26.4$ and the turn-over time $\tau_{exp} = 1.14s$. The scalar dissipation rate is evaluated to approximately $\epsilon_\theta \simeq 10^{-2}\,{}^\circ C^2.s^{-1}$ for a scalar gradient $\beta = 1.78{}^\circ C.m^{-1}$. Assuming that for this experiment the Prandtl number is about 0.7, a reference fluctuating scalar gradient is computed as

$$\Lambda_{\rm ref} = \left(\frac{\partial\theta}{\partial x}\right)_{ref} = \sqrt{\frac{\epsilon_\theta}{3a}},$$

so that the dimensionless mean scalar gradient is $\mathcal{S}_\theta = \beta/\Lambda_{\rm ref} = 0.152$. Temporal results are transposed to spatial ones through

$$\frac{x}{M} = \frac{t}{\tau_0}\frac{U\tau_{exp}}{M}\ ,$$

where $\tau_0$ is the kinetic characteristic time $K/\epsilon$ evaluated numerically after two turn-over times, so that transition effects from the initial conditions are erased. The experimental decay rate of the kinetic field being $\alpha_{exp} = -1.3$, Saffman turbulence ($\sigma = 2$) is an appropriate large scales initial condition for the EDQNM simulations. The cospectrum correlation

$$\rho_{u_i\theta} = \frac{< u_i\theta >}{\sqrt{< u_i^2 >< \theta^2 >}}, \qquad \rho_{w\theta} = \rho_{u_3\theta}, \tag{4.10}$$

is well-recovered and $\rho_{w\theta} \to -0.7$. The ratio of scalar production $-\Lambda K_\mathcal{F}$ and dissipation $\epsilon_T$ is also in agreement with present results. The final value of the characteristic times ratio

$$R_T = \frac{K\,\epsilon_T}{K_T\,\epsilon} \tag{4.11}$$

matches quite well with experimental data. However, there is a slight difference for the ratio of integral scales $L_T/L$ ($\simeq 0.7$ with the present anisotropic EDQNM closure, and $\simeq 0.9$ experimentally). As no indications are given, there could simply be a difference in the definitions. Nevertheless, the fact that $L_T(t) < L(t)$ is recovered. Let's underline that the

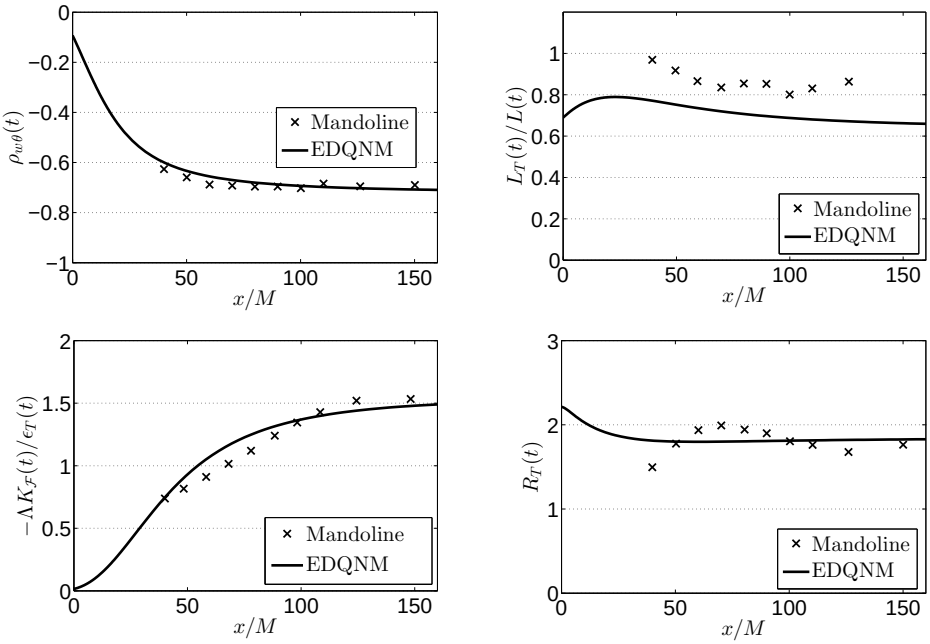


FIGURE 4. Comparisons with experimental results of Sirivat & Warhaft (1983) for the case of the mandoline, as a function of $x/M$, where $M$ is the meshsize and $x$ the distance to the grid. $\times$ correspond to the experimental results and lines to the EDQNM ones. Top row: the cospectrum correlation $\rho_{w\theta}$ defined in (4.10) at left. At right the scalar to kinetic integral scales ratio $L_T/L$. Bottom row: ratio of production and dissipation of the passive scalar $-\Lambda K_{\mathcal{F}}/\epsilon_T$ at left. At right, kinetic to scalar time scales ratio $R_T$ defined in (4.11).

initial condition is isotropic here, which is not the case in the experiment: as mentioned by Sirivat & Warhaft (1983), the initial fluctuating temperature field is slightly inhomogeneous, and because of the grid itself the kinetic field contains some anisotropy. But still, the early times of $\rho_{w\theta}$ and $-\Lambda K_{\mathcal{F}}/\epsilon_T$ are well captured. About the cospectrum correlation $\rho_{w\theta}$, it has to be pointed out that there exists a large scatter, since measured values span from $\simeq -0.19$ to $\simeq -0.8$, with an average around $\simeq -0.65$ (Venkataramani & Chevray 1978; Sirivat & Warhaft 1983; Overholt & Pope 1996; Mydlarski 2003). It appears in EDQNM simulations that $\rho_{w\theta}$ strongly varies for $5 \leqslant Re_\lambda \leqslant 300$, roughly from 0.6 for high Reynolds to $\simeq 0.71$ for low Reynolds. This is the classical range of Reynolds numbers covered by experiments and DNS. Consequently, the reason for the scattering of $\rho_{w\theta}$ could be moderate Reynolds numbers, where it becomes more sensitive to the intensity of the mean-scalar gradient.

### 4.2. *Homogeneous shear turbulence (HST)*

In this section, qualitative comparisons and general results are given for the passive scalar field submitted to a shear without any scalar gradient. This particular framework has not received much attention in experiments or DNS unlike the case with both velocity and scalar gradients that will be addressed in the next section. Firstly, the case of an anisotropy imposed at short times only and then released is investigated, and finally, the emphasis is put on the passive scalar field submitted to a sustained shear. For a shear-driven flow, the mean velocity gradient matrix is written $A_{13} = dU_1/dx_3 = -S$ with $S > 0$. The dimensionless time $St$ refers to the quantity of anisotropy injected in

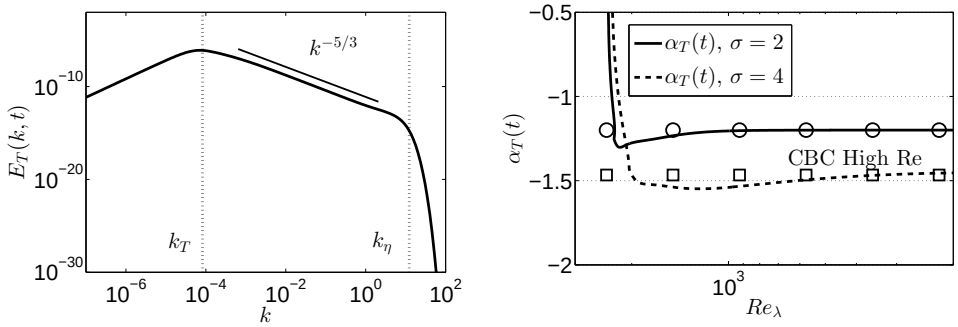


FIGURE 5. At left, scalar spectrum $E_T(k,t)$ in a sustained shear flow, with $St = 50$ ($Re_\lambda = 10^4$) and $\sigma = 2$, along with the scalar integral and Kolmogorov wavenumbers $k_T$ and $k_\eta$, as a function of the wavenumber $k$. At right, scalar decay exponents $\alpha_T$ in high Reynolds numbers regime, with $St = 1$ for $\sigma = 2$ and $\sigma = 4$, as a function of the Reynolds number $Re_\lambda$. Symbols represent the theoretical values expected from (4.12): $\circ$ is for $\sigma = \sigma_T = 2$ and $\square$ for $\sigma = \sigma_T = 4$.

the flow. In both cases, the scalar spectrum displays a $k^{-5/3}$ inertial-convective range as revealed in figure 5.

4.2.1. *Case of the shear-released turbulence*

In isotropic turbulence, the decay exponents of scalar integrated quantities such as the scalar variance $K_T$ and the scalar dissipation rate $\epsilon_T$ are well-known since Comte-Bellot & Corrsin (1966) and are recalled in Table 3 following the work of Briard *et al.* (2015). For the scalar variance

$$K_T(t) \sim t^{\alpha_T}, \qquad \alpha_T = -2\frac{\sigma_T - p_T + 1}{\sigma - p + 3}, \tag{4.12}$$

where $p_T(\sigma = \sigma_T = 4) = 0.27$ and $p_T(\sigma = \sigma_T \leqslant 3) = 0$, and $p(\sigma = 4) = 0.55$ and $p(\sigma \leqslant 3) = 0$. These parameters $p$ and $p_T$ reflect the strong backscatter of energy for the velocity and scalar fields respectively, that can occur in the infrared range notably for the Batchelor case. In particular, $p_T$ slightly depends on the Prandtl number and much more on the kinetic infrared slope $\sigma$ (Briard *et al.* 2015). In figure 5, large Reynolds numbers scalar decay exponents are recovered for Saffman and Batchelor shear-released turbulence. This means that initial large scales velocity gradients do not alter the long-time decay of scalar integrated quantities. Such a result for the scalar field is similar to what was found for the velocity one (Briard *et al.* 2016).

Before the release of the velocity gradients $S = 1\tau_0^{-1}$ at $t = 1\tau_0$, the scalar anisotropy indicators $b_{ij}^T$ depart from the isotropic value 0. Then the passive scalar field experiences a return to isotropy (RTI) mechanism driven by the velocity field. This process is displayed in figure 6. An asymptotic anisotropic state is reached, similar to the kinetic one (Speziale *et al.* 1990; Mons *et al.* 2016). The final non-zero values of $b_{ij}^T$ show that there is still anisotropy in the flow after the release of the velocity gradients $A_{ij}$. The spectral anisotropy tensors $H_{ij}^{(T)}(k,t)$ are also displayed in figure 6, and reveal that anisotropy is mostly gathered around the scalar integral wavenumber $k_T$. The interesting point is that some anisotropy persists in the small scales of the scalar second-order moments, as shown in the zoom. Simulations indicate that small scales of the velocity second-order moments are completely isotropic. This is in agreement with most of DNS and experiments.

A supplementary qualitative comparison, in the case of anisotropy-released flow for the passive scalar field, can be done. Indeed, an axisymmetric contraction is performed by Gylfason & Warhaft (2009), where the temperature fluctuations are created by a

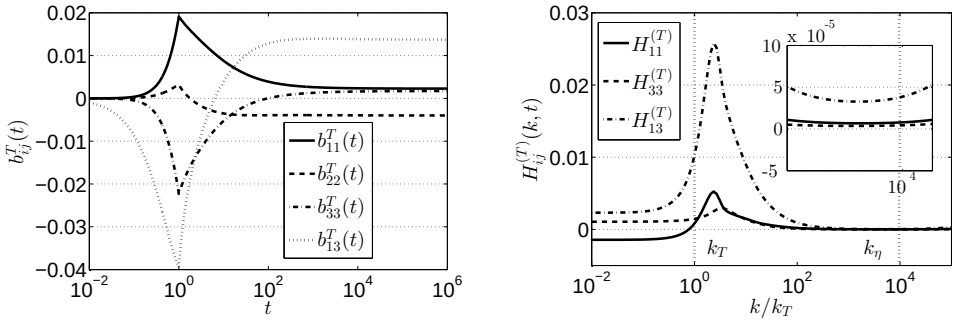


FIGURE 6. Scalar anisotropy indicators for $\sigma = 2$, with $St = 1$. At left, $b_{ij}^T(t)$, defined in (3.5), as a function of time $t$. At right, $H_{ij}^{(T)}(k,t)$, defined in (3.3), at $t = 10^6\tau_0$ ($Re_\lambda = 800$), along with the scalar integral and Kolmogorov wavenumbers $k_T$ and $k_\eta$, as a function of the normalized wavenumber $k/k_T$.

mean gradient. Although no quantitative comparison is possible because of the moderate anisotropy limitation of the present model (the dimensionless velocity gradient reaches $\mathcal{S} = 70$ in Gylfason & Warhaft (2009)), interesting qualitative facts can be reported. The measure of anisotropy is done using the fluctuating scalar covariance $C_{ij} =< \xi_i\xi_j >$, where $\xi_i = \partial\theta/\partial x_i$, which brings the same kind of information as the $b_{ij}^T$ do. During the contraction, $|C_{ij}|$ increases, and at the exit of the contraction, it converges to a constant value, different from zero. This behaviour is similar to the one of the $b_{ij}^T$, and Gylfason & Warhaft (2009) concluded that there is a partial return to isotropy, which is in agreement with the present results.

4.2.2. *Case of the sustained-shear turbulence*

In this part, the shear is maintained. It is known that there is an exponential growth of the kinetic energy $K(t)$ due to non-linear transfers (De Souza *et al.* 1995; Garg & Warhaft 1998; Brethouwer 2005; Sagaut & Cambon 2008; Mons *et al.* 2016). The kinetic exponential growth rate is

$$\gamma = 2b_{13} - \frac{\epsilon}{KS}, \tag{4.13}$$

which directly comes from the evolution equation of $K(t)$, where $b_{13} = R_{13}/(2K)$. The estimation due to the present modelling (Mons *et al.* 2016) gives $\gamma \simeq 0.34$. This seemingly high value of $\gamma$ is discussed in Briard *et al.* (2016). The relevant question is now: is there a similar growth for the scalar variance $K_T(t)$? Its evolution is governed by the equation

$$\frac{dK_T}{dt} = 2\Lambda K_{\mathcal{F}}(t) - \epsilon_T(t). \tag{4.14}$$

In HST, $\Lambda = 0$ and there is no production term linked to velocity gradients unlike the evolution equation of $K(t)$. Hence, there should be no growth of $K_T(t)$ even if the shear is maintained. In figure 7, the $b_{ij}^T$ and the scalar shear rapidity

$$S_R^T(t) = \frac{\epsilon_T(t)}{SK_T(t)} \tag{4.15}$$

reach constant values for $St \geqslant 30$. Moreover, it can be seen in figure 7 that the scalar variance $K_T$ decreases exponentially, with a decay rate $\gamma_T \simeq -0.52$. Let's replace $K_T$ and $\epsilon_T$ in (4.14) by

$$K_T(t) = K_T^\infty \exp(\gamma_T St), \qquad \epsilon_T(t) = \epsilon_T^\infty \exp(\gamma_T St).$$

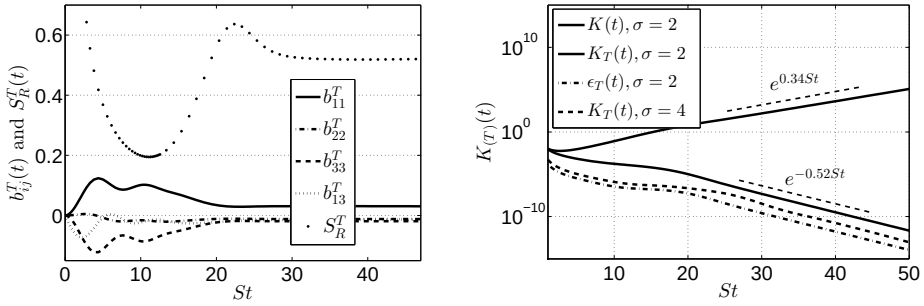


FIGURE 7. Evolution of integrated quantities in HST, as a function of the accumulated anisotropy $St$, with $S = 1\tau_0^{-1}$, and $Re_\lambda(St = 50) \sim 10^4$. At left, scalar anisotropy indicators $b_{ij}^T$, defined in (3.5), along with $S_R^T = \epsilon_T/(K_T S)$ for $\sigma = 2$. At right, kinetic and scalar energies $K$ and $K_T$, and scalar dissipation rate $\epsilon_T$, for $\sigma = 2$ and $\sigma = 4$.

An analytical expression for $\gamma_T$ is then obtained:

$$\gamma_T = -\frac{\epsilon_T^\infty}{SK_T^\infty}, \qquad K_T(t) \sim K_T(0)\exp(\gamma_T St). \tag{4.16}$$

The decay rate $\gamma_T$ found by plotting $K_T$ is in good agreement with the asymptotic value of $S_R^T$, which also gives $\gamma_T = -0.52$. The important result here is that the value of the scalar exponential decay rate $\gamma_T$ seems not to depend on the shear rate $S$ for moderate intensity, nor on the infrared exponents $\sigma$ and $\sigma_T$ (and neither does $\gamma$ for the exponential growth of $K(t)$ (Briard *et al.* 2016)). The scalar dissipation $\epsilon_T$, also displayed in figure 7, exponentially decreases with the same rate $\gamma_T = -0.52$, which is consistent with the evolution equation (4.14).

The fact that anisotropy created by mean velocity gradients accelerates the decay of the scalar field has been observed experimentally by Warhaft (1980) with a contraction. Moreover, such an exponential decrease of the scalar variance $K_T$ has been found theoretically by Gonzalez (2000) using a self-preservation analysis. The exponential decay rate obtained is $\beta'_\theta = -(S\tau_\theta)^{-1}$ with $\tau_\theta = K_T/\epsilon_\theta$ which is precisely the $\gamma_T$ obtained here.

Various simulations show that the realizability condition (3.23) is violated at the scalar level for $S > 3\tau_0^{-1}$, whereas it still holds at the velocity level. This shows that pure shear flows might be a limit case of the present anisotropic EDQNM modelling for the passive scalar dynamics. Hopefully, this case is less studied and less representative of atmospheric flows than the HSTSG one which is the topic of the next part: when a mean scalar gradient is added to the mean shear, the large scale anisotropy at the scalar level is smoothed and the scalar field can handle higher shear rates.

### 4.3. *Homogeneous shear turbulence with a mean scalar gradient (HSTSG)*

This final part focuses on homogeneous shear turbulence with a mean scalar gradient (HSTSG). The emphasis is put on the impact of both mean velocity and scalar gradients on the scalar flux and the passive scalar.

#### 4.3.1. *Definitions and transfers*

Previously, it was shown that with a mean scalar gradient $\lambda_3$, only the third component of the scalar flux $E_3^F = \mathcal{F}$ was non-zero. With a velocity gradient only, no scalar flux appears at all. With both velocity and scalar gradients, the first component of the scalar flux is also non-zero. Therefore, the streamwise flux is defined as

$$E_1^F(k,t) = \mathcal{F}_S(k,t), \tag{4.17}$$

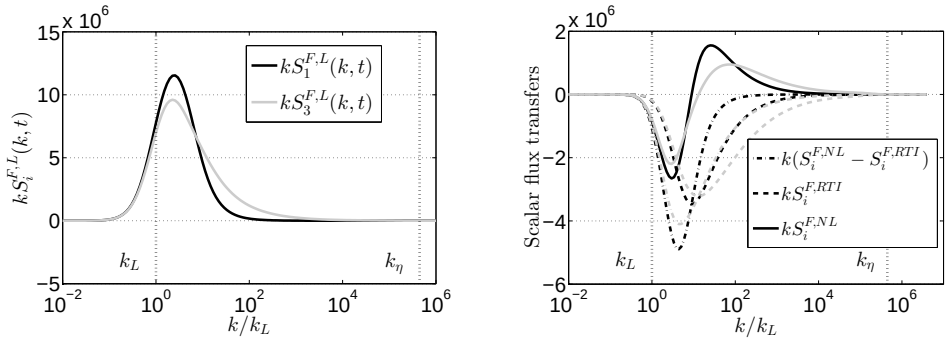


FIGURE 8. Linear (at left) and non-linear (at right) transfers for the cospectrum ($i = 3$, grey) and streamwise flux ($i = 1$, black) for $\sigma = 2$ at $St = 50$, where $Re_\lambda = 2.10^4$, and as a function of the normalized wavenumber $k/k_L$.

which arises only with the additional presence of a velocity gradient $dU_1/dx_3$. Its energy and dissipation rate are then

$$K_{\mathcal{F}}^S(t) = \int_0^\infty \mathcal{F}_S(k,t)dk, \qquad \epsilon_{\mathcal{F}}^S(t) = (\nu + a)\int_0^\infty k^2 \mathcal{F}_S(k,t)dk. \tag{4.18}$$

In figure 8, both linear and non-linear spherically averaged transfers are presented for the cospectrum and the streamwise flux. One can note that they are very similar and only slightly vary in intensity. This shows that the two components of the scalar flux behave similarly in HSTSG. The small scales return to isotropy of scalar second-order moments in the HSTSG framework is discussed later, and the spectral scaling of $\mathcal{F}_S$ is addressed after the comparisons.

4.3.2. *Comparison with Rogers* et al. *(1989)*

Now, the comparison is made with the DNS of Rogers *et al.* (1989). There, the velocity gradient $dU_1/dx_2$ is such that the dimensionless shear rate is $\mathcal{S} = 14.142$, so that $dU_1/dx_2 = S = \mathcal{S}\tau_0^{-1}$ (see De Souza *et al.* (1995) for the process). Three cases for the scalar gradient are performed, one in each direction $x_1$, $x_2$ and $x_3$, with the dimensionless mean scalar gradient $\mathcal{S}_\theta = 2.5$. Comparisons are made with the diffusivity tensor

$$D_{ij}(t) = - < \theta u_i > \left(\frac{dT}{dx_j}\right)^{-1}. \tag{4.19}$$

Each column of the tensor $D_{ij}$ refers to a different simulation where the direction of the scalar gradient changes. For instance, $D_{13}$ refers to the third case. The agreement between EDQNM simulations and DNS is revealed in figure 9 where $D_{ij}$ is normalized by $D_{22}$. A difference is observed along the flow direction for $D_{11}/D_{22}$ where DNS predicts a higher value. This discrepancy may come from the limited DNS resolution that alters the dynamics in the streamwise direction. Then, for each simulation, the turbulent Prandtl number is defined as

$$Pr_T(t) = -\frac{R_{12}}{SD_{ii}}, \qquad \text{with no summation on } i\ , \tag{4.20}$$

where $D_{ii}$ is the turbulent diffusivity, with $i = 1$, 2 or 3 depending on the case considered. The agreement is rather good: the asymptotic value of $Pr_T \simeq 0.8$ is recovered in the second case, whereas the general behaviour is captured for the first and third cases: $Pr_T^{(1)} < Pr_T^{(3)} < Pr_T^{(2)}$.

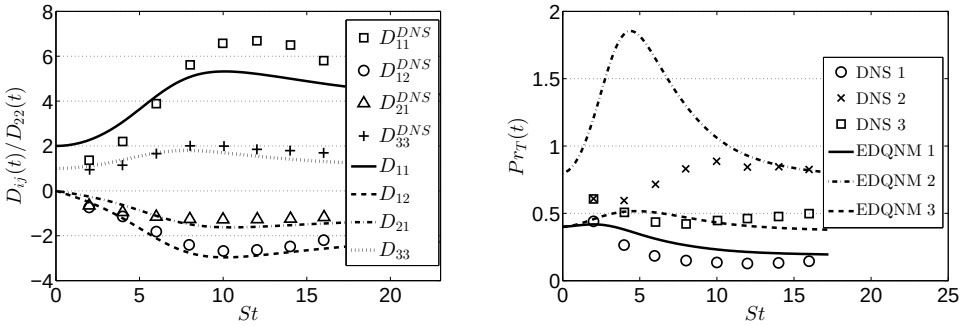


FIGURE 9. Comparisons with numerical results of Rogers *et al.* (1989), with $\sigma = 2$, $\mathcal{S} = 14.142$ and $\mathcal{S}_\theta = 2.5$, as a function of the accumulated anisotropy $St$. Symbols correspond to the DNS, and lines to the EDQNM simulations. At left, the normalized diffusivity tensor, defined in (4.19), for the three orientations of the mean scalar gradient. At right, the turbulent Prandtl number $Pr_T$, defined in (4.20), for these three cases

4.3.3. *Comparison with Kassinos* et al. *(2007)*

A last comparison is performed with the more recent DNS of Kassinos *et al.* (2007). This work deals about magnetohydrodynamics (MHD) but the validation is made in the purely hydrodynamic case with the data of Brethouwer (2005). Hence, only the case where the magnetic field is zero and where there is no rotation is considered. The mean velocity and scalar gradients are along $x_2$ and such that $\mathcal{S} = 8.95$ and $\mathcal{S}_\theta = 1$. The kinetic field is allowed to decay without any forcing before velocity and scalar gradients are applied at $t_0$. There, the Reynolds number is $Re_\lambda = 45$ with $SK/\epsilon(t = t_0) = 18$. The scalar fluctuations are set to 0 at $t = t_0$ (this is why initially $\rho_{v\theta}(t = t_0) = -1$). For EDQNM simulations, the mean gradients are applied after two turn-over times and there $SK/\epsilon = 13$ and $Re_\lambda = 50$. The two correlations $\rho_{u\theta}$ and $\rho_{v\theta}$ are presented in figure 10 along with

$$\beta = \frac{S}{\Lambda}\sqrt{\frac{3K_T}{2K}}, \tag{4.21}$$

which characterizes the relative strengths of the velocity and scalar fluctuations. There is a good agreement for the asymptotic values of $\rho_{u\theta}$ and $\rho_{v\theta}$, and the transitory behaviours are rather well-captured. The weaker value for $\rho_{u\theta}$ at moderate $St$ may be the consequence of a slightly too strong increase for our $R_{11} =< u_1 u_1 >$. This does not prevent to reach the correct value at larger $St$ in the asymptotic state. As for $\beta$, the simulation slightly differs from the DNS: the $\beta$ value is over-estimated and has almost reached a constant value whereas it slightly decreases for Kassinos *et al.* (2007). Nevertheless, in both cases $\beta \sim 1$ at large $St$, which indicates that the velocity and scalar fluctuations have a similar contribution to the anisotropic asymptotic state.

An additional comparison with the pioneering experiment of Tavoularis & Corrsin (1981) is proposed in Appendix B: this comparison does not appear in the core of the text since it investigates quantities such as $\rho_{u_i\theta}$, $\beta$ and $Pr_T$ that have already been studied here. Nevertheless, this experimental work is an important historical contribution, often used as a basis of comparisons, that deserve to be addressed.

### 4.4. *Conclusion on the comparisons*

The present anisotropic EDQNM modelling for the passive scalar and its flux has been compared with several experiments and DNS. The agreement between asymptotic values of integrated quantities, and even sometimes in the transitory state, validate the mod-

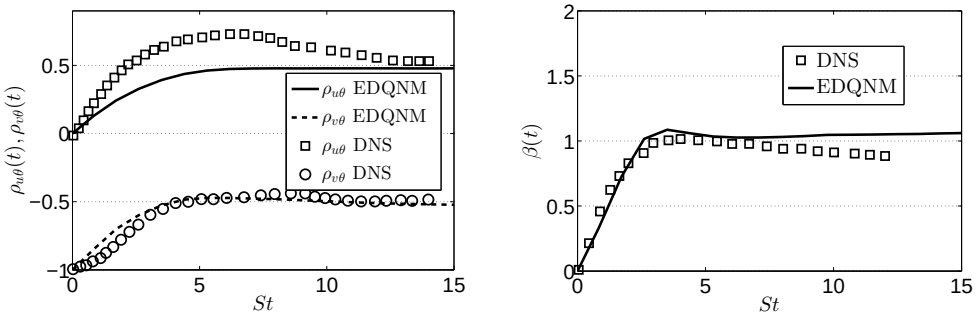


FIGURE 10. Comparisons with the numerical results of Kassinos *et al.* (2007), for $\sigma = 2, \mathcal{S} = 8.95$ and $\mathcal{S}_\theta = 1$, as a function of the accumulated anisotropy $St$. Symbols correspond to DNS and lines to EDQNM simulations. Both $\rho_{u\theta}$ and $\rho_{w\theta}$, defined in (4.10), are investigated at left. At right, $\beta$ defined in (4.21).

elling introduced in §2 and §3. Nevertheless, it has to be mentioned that the present model seems to slightly under-estimate the turbulent Prandtl number.

## 5. Decay and growth laws in homogeneous anisotropic turbulence

In this section, the anisotropic EDQNM modelling is used to address the high Reynolds numbers regimes of HAT. This part focuses on the the decay and growth of the cospectrum energy and scalar variance in HITSG. From a physical point of view, informations about the dominant mechanisms during the decay are brought. Moreover, the scaling of the scalar spectra are investigated and the small scales anisotropy is discussed for both HITSG and HSTSG.

### 5.1. *Decay and growth laws in HITSG*

The results presented here are an extension of an analysis previously applied to the passive scalar in HIT (Briard *et al.* 2015). The theoretical decay exponents of kinetic and scalar integrated quantities are recalled in Table 3.

The cospectrum $\mathcal{F}$ is continuously destroyed by the decay of the velocity field, and is consequently also decaying. Theoretical decay exponents can be derived similarly to what Comte-Bellot and Corrsin did for the passive scalar. Two assumptions, based on physical arguments for high Reynolds numbers, are needed. Firstly, figure 2 revealed that the cospectrum infrared dynamics is driven only by the kinetic one. Then, we assume that the main contribution to the decay mechanism comes from the inertial range and consequently, that only the $k^{-7/3}$ inertial range should be taken into account to determine the decay exponents of $\mathcal{F}$. Secondly, in the case of Batchelor turbulence, when the permanence of large eddies hypothesis is broken, backscatter parameters $p$ and $p_T$ are introduced for the velocity and scalar fields respectively in HIT (Briard *et al.* 2015). Since $\mathcal{F}$ is the spectral counterpart of the velocity-scalar cross correlation, its backscatter parameter $p_\mathcal{F}$ should contain both effects. Hence, one defines $p_\mathcal{F} = (p + p_T)/2$ for $\sigma = 4$ (so that $p_\mathcal{F} = 0$ for $\sigma \leqslant 3$). This gives $p_\mathcal{F} = 0.4075$ in the case $Pr = 1$ for $\sigma = 4$. These reasonable assumptions yield

$$K_\mathcal{F}(t) \sim \int_{k_L}^{\infty} \mathcal{F}(k,t)dk \sim k_L^{-4/3}\epsilon^{1/3}. \tag{5.1}$$

Injecting in this equation the decay exponents of $\epsilon$ and $k_L$ recalled in Table 3, and using

| | High Reynolds regime | Low Reynolds regime |
|---|---|---|
| $K(t)$ | $\alpha = -2\frac{\sigma-p+1}{\sigma-p+3}$ | $\alpha = -\frac{\sigma+1}{2}$ |
| $\epsilon(t)$ | $n_\epsilon = -3\frac{\sigma-p+5/3}{\sigma-p+3}$ | $n_\epsilon = -\frac{\sigma+3}{2}$ |
| $L(t)$ and $L_T(t)$ | $n_L = \frac{2}{\sigma-p+3}$ | $n_L = \frac{1}{2}$ |
| $K_T(t)$ | $\alpha_T = -2\frac{\sigma_T-p_T+1}{\sigma-p+3}$ | $\alpha_T = -\frac{\sigma_T+1}{2}$ |
| $\epsilon_T(t)$ | $n_{\epsilon_T} = -\frac{\sigma-p+5+2\sigma_T-2p_T}{\sigma-p+3}$ | $n_{\epsilon_T} = -\frac{\sigma_T+3}{2}$ |
| $Re_\lambda$ | $n_{Re_\lambda} = -\frac{1}{2}\frac{\sigma-p-1}{\sigma-p+3}$ | $n_{Re_\lambda} = -\frac{\sigma-1}{8}$ |

TABLE 3. Kinetic and scalar decay exponents in homogeneous isotropic turbulence. $\sigma$ and $\sigma_T$ are the kinetic and scalar infrared slopes. $p$ and $p_T$ are the kinetic and scalar backscatter parameters. $Re_\lambda = K\sqrt{20/3\nu\epsilon}$ is the Reynolds number based on the Taylor micro-scale. The kinetic and scalar integrated quantities are: kinetic energy $K = \int E dk$; kinetic energy dissipation rate $\epsilon = 2\nu \int k^2 E\, dk$; kinetic integral scale $4L = 3\pi K^{-1} \int k^{-1} E\, dk$; scalar variance $K_T = \int E_T\, dk$; scalar variance dissipation rate $\epsilon_T = 2a \int k^2 E_T\, dk$; scalar integral scale $2L_T = \pi K_T^{-1} \int k^{-1} E_T\, dk$.

$p_\mathcal{F}$, one obtains the theoretical decay exponent of the cospectrum for high Reynolds numbers

$$K_\mathcal{F}(t) \sim t^{\alpha_\mathcal{F}}, \qquad \alpha_\mathcal{F} = -\frac{\sigma - p_\mathcal{F} - 1}{\sigma - p + 3}. \tag{5.2}$$

In the low Reynolds numbers regime, when the cospectrum survives, the production term $P_\mathcal{F}$ drives the dynamics of the velocity-scalar correlation. The return to isotropy term $\Pi_\mathcal{F}$, and the cospectrum dissipation rate $\epsilon_\mathcal{F}$, can be considered as negligible. Indeed, considering the form of the cospectrum dissipation (4.4), this quantity reaches its highest values in the inertial range, which tends to disappear for low Reynolds numbers. Therefore, the evolution equation (4.5) of the cospectrum energy becomes $(dK_\mathcal{F}/dt) \sim P_\mathcal{F} = 2\Lambda K/3$. This immediately yields

$$\alpha_\mathcal{F} = -\frac{\sigma - 1}{2}, \tag{5.3}$$

which does not depend on the scalar gradient $\Lambda$.

These theoretical decay exponents for the cospectrum for high and low Reynolds numbers are assessed numerically in figure 11. The agreement is excellent, even for the particular case of Batchelor turbulence. Such laws could not have been observed before since it requires high Reynolds numbers in decaying turbulence, whereas most of the DNS of HITSG consider a stationary velocity field at moderate Reynolds numbers. These theoretical results, assessed numerically, give further insights into the prediction of high Reynolds numbers decay in HITSG. From (5.2) and (5.3), it follows that $K_\mathcal{F}$ does not decay for $\sigma = 1$. In this case, the Reynolds number $Re_\lambda$ remains constant and so the dynamics of the inertial range, on which is based $\alpha_\mathcal{F}$, remains unchanged.

The dissipation rate $\epsilon_\mathcal{F}$ is now investigated. Probably because the scalar flux is a purely anisotropic quantity, which implies that $\epsilon_\mathcal{F}$ is not conserved in the inertial range unlike $\epsilon$ and $\epsilon_T$, one cannot express its time dependence as a power law. Nevertheless, as the

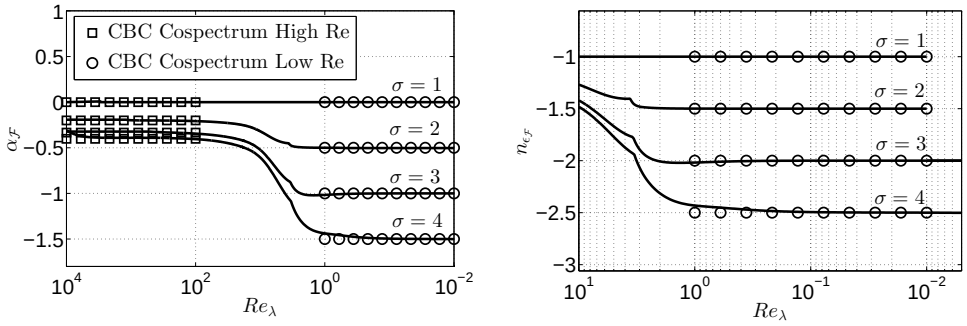


FIGURE 11. Decay exponents of the cospectrum energy $\alpha_{\mathcal{F}}$ at left, and of the cospectrum dissipation $n_{\epsilon_{\mathcal{F}}}$ at right for different infrared slopes $\sigma$, as a function of the Reynolds number $Re_\lambda$. Symbols represent theoretical predictions: □ for high Reynolds numbers, given by (5.2); ∘ for low Reynolds numbers, given by (5.3) and (5.4).

inertial range disappears for low Reynolds numbers, obtaining the decay exponent $n_{\epsilon_{\mathcal{F}}}$ of $\epsilon_{\mathcal{F}}$ is possible in this regime, considering the evolution equation (4.5) so that

$$\epsilon_{\mathcal{F}}(t) \sim t^{n\epsilon_{\mathcal{F}}}, \qquad n_{\epsilon_{\mathcal{F}}} = \alpha_{\mathcal{F}} - 1 = -\frac{\sigma+1}{2}. \tag{5.4}$$

The agreement between this theoretical result and numerical simulations is displayed in figure 11 as well.

The emphasis is now put on the effect of the mean scalar gradient $\Lambda$ on the passive scalar itself. The scalar spectrum still displays a $k^{-5/3}$ inertial-convective range despite the mean gradient, as revealed in figure 1, and this was obtained experimentally as well (Mydlarski & Warhaft 1998). From the evolution equation of the scalar variance (4.14), it follows that the dynamics of $K_T$ is driven by the production term in the presence of a mean scalar gradient $\Lambda$. Using the previous results regarding the decay exponents of $K_{\mathcal{F}}$, the theoretical exponent of $K_T$ in presence of a mean scalar gradient $\alpha_T^\Lambda$ can be found. In the high Reynolds numbers regime, one has

$$K_T(t) \sim t^{\alpha_T^\Lambda}, \qquad \alpha_T^\Lambda = \frac{4 + p_{\mathcal{F}} - p}{\sigma - p + 3} > 0, \tag{5.5}$$

and for low Reynolds numbers

$$\alpha_T^\Lambda = -\frac{\sigma - 3}{2}. \tag{5.6}$$

Note that the exponents do not depend explicitly on the scalar gradient $\Lambda$. The agreement between these theoretical expressions of $\alpha_T^\Lambda$ and numerical simulations is presented in figure 12 in both high and low Reynolds numbers regimes. For high Reynolds numbers, the scalar variance grows in time whatever $\sigma$ is, whereas for low Reynolds numbers, it decays only for $\sigma = 4$. This can be explained using some physical arguments. The theoretical prediction (5.6) of $\alpha_T^\Lambda$ is based on the fact that the dynamics of $K_T$ is driven by the production term $2\Lambda K_{\mathcal{F}}$, and $K_{\mathcal{F}}$ is greater for smaller $\sigma$. Consequently, for high infrared slope such as $\sigma = 4$, the spectrum $E(k,t)$, and thus $\mathcal{F}(k,t)$, has less energy in large scales, resulting into a weak production term for the scalar variance that does not balance dissipation. This is consistent with HITSG experimental results at moderate $Re_\lambda$, where the scalar variance can grow or decay depending on the intensity of $\Lambda$: with a weak $\Lambda$, $K_T$ still decays (nevertheless more slowly than in HIT). Therefore, a strong mean scalar gradient $\Lambda$ corresponds to a small infrared slope $\sigma$, or equivalently corresponds to energetic large scales.

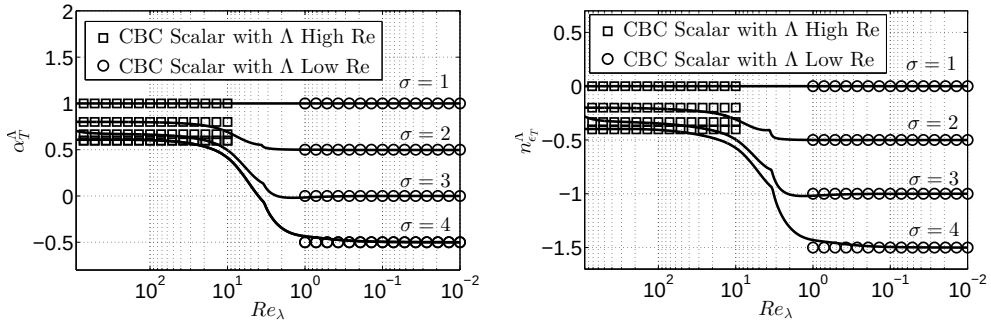


FIGURE 12. Growth and decay exponents of the scalar energy $\alpha_T^\Lambda$ at left, and of the scalar dissipation rate $n_{\epsilon_T}^\Lambda$ at right for different infrared slopes $\sigma$, as a function of the Reynolds number $Re_\lambda$. Symbols represent theoretical predictions: □ for high Reynolds numbers, given by (5.5); ∘ for low Reynolds numbers, given by (5.6).

| | High Reynolds regime $\forall(\Lambda, \sigma_T)$ | Low Reynolds regime $\forall(\Lambda, \sigma_T)$ |
|---|---|---|
| $K_T(t)$ | $\alpha_T^\Lambda = \frac{4+p_\mathcal{F}-p}{\sigma-p+3}, \quad p_\mathcal{F} = \begin{cases} 0 & ,\sigma \leqslant 3 \\ \frac{1}{2}(p+p_T) & ,\sigma = 4 \end{cases}$ | $\alpha_T^\Lambda = -\frac{\sigma-3}{2}$ |
| $\epsilon_T(t)$ | $n_{\epsilon_T}^\Lambda = \alpha_\mathcal{F} = -\frac{\sigma-p_\mathcal{F}-1}{\sigma-p+3}$ | $n_{\epsilon_T}^\Lambda = \alpha_\mathcal{F} = -\frac{\sigma-1}{2}$ |
| $K_\mathcal{F}(t)$ | $\alpha_\mathcal{F} = -\frac{\sigma-p_\mathcal{F}-1}{\sigma-p+3}$ | $\alpha_\mathcal{F} = -\frac{\sigma-1}{2}$ |
| $\epsilon_\mathcal{F}(t)$ | not defined | $n_{\epsilon_\mathcal{F}} = -\frac{\sigma+1}{2}$ |

TABLE 4. Decay and growth exponents of integrated quantities in HITSG for the cospectrum and scalar fields. $\sigma$ is the kinetic infrared slope. $p$, $p_T$ and $p_\mathcal{F}$ are the backscatter parameters. $\alpha_\mathcal{F}$ and $\alpha_T^\Lambda$ are the algebraic exponents of the cospectrum energy $K_\mathcal{F}$ and the scalar variance $K_T$, given in (5.2), (5.3), (5.5), and (5.6). $n_{\epsilon_\mathcal{F}}$ and $n_{\epsilon_T}^\Lambda$ are the algebraic exponents of their corresponding dissipation rates, given in (5.4) and (5.7).

In the particular case of Saffman turbulence ($\sigma = 2$), the value $\alpha_T^\Lambda = 4/5$ was already found by Chasnov (1995). There, the decay and growth laws of passive and active scalar fields, with and without buoyancy or mean gradient, are studied. Power laws for the active scalar field were assessed by large eddy simulations (LES). Hence, the present EDQNM simulations validate the power laws for the passive scalar field, with an explicit dependence on the initial large scales conditions $\sigma$. Consequently, this analysis can be considered as an extension of Chasnov (1995) regarding the growth of a passive scalar in HITSG.

Then, from the scalar variance evolution equation (4.14), the scalar dissipation should evolve in time similarly as the cospectrum energy,

$$\epsilon_T(t) \sim t^{n_{\epsilon_T}^\Lambda}, \qquad n_{\epsilon_T}^\Lambda = \alpha_\mathcal{F}, \tag{5.7}$$

in both high and low Reynolds numbers regimes. This is assessed in figure 12 as well. All the new results regarding the growth or decay predictions for $K_\mathcal{F}$, $K_T$, $\epsilon_\mathcal{F}$ and $\epsilon_T$ are gathered in Table 4.

As a conclusion, the dynamics of a scalar field forced by a mean gradient is fully

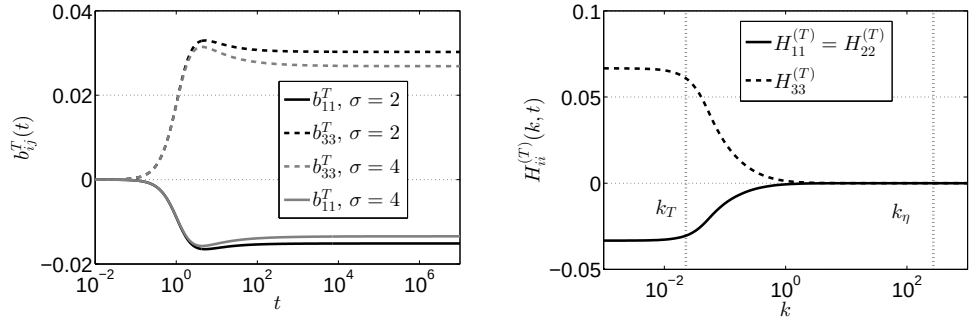


FIGURE 13. At left, diagonal components of $b_{ij}^T$, defined in (3.5), for both Saffman (black) and Batchelor (grey) turbulence, as a function of time $t$. At right, diagonal components of $H_{ij}^{(T)}$, defined in (3.3), at $Re_\lambda = 10^3$ for $\sigma = 2$, along with the Kolmogorov and scalar integral wavenumbers $k_\eta$ and $k_T$, as a function of the wavenumber $k$.

dominated by the decaying isotropic kinetic field. Indeed, the initial scalar large scales condition $\sigma_T$ never appears in the theoretical decay and growth exponents. The velocity field completely leads the dynamics of the flow. This is consistent with a similar result obtained by De Marinis *et al.* (2013) in HIT, where the passive scalar field experiences a Joule heat production. Therefore, it can be concluded that with a production mechanism, the velocity field completely dominates the passive scalar dynamics.

With these new algebraic exponents for $K_T$ and $K_\mathcal{F}$, one can show that for high or low Reynolds numbers, *i.e.* when both $\alpha_\mathcal{F}$ and $\alpha_T^\Lambda$ are recovered, the correlation $\rho_{w\theta}$ previously investigated is independent of time. Indeed, its algebraic exponent is then $\alpha_\mathcal{F} - (\alpha + \alpha_T^\Lambda)/2 = 0$. This means that for moderate Reynolds numbers ($Re_\lambda \sim 100$) not high enough to ensure that $\alpha_\mathcal{F}$ and $\alpha_T^\Lambda$ are verified, $\rho_{w\theta}$ varies in time. This could be the reason for the scattering of the obtained values for $\rho_{w\theta}$ in DNS and experiments, pointed out in section 4.

### 5.2. *Return to isotropy in HITSG*

The small scales return to isotropy (RTI) is briefly investigated for the HITSG configuration, at the level of the scalar second-order moments. Since only the third component of the scalar gradient is non-zero, this is an axisymmetric configuration, meaning that the scalar anisotropy indicators verify $2b_{11}^T = 2b_{22}^T = -b_{33}^T$, and $2H_{11}^{(T)} = 2H_{22}^{(T)} = -H_{33}^{(T)}$. In figure 13, the $b_{ij}^T$ are presented: they become constant both in Saffman and Batchelor turbulence, which is qualitatively the same behaviour as the $b_{ij}$ in a sustained shear flow. The spectral anisotropy tensors $H_{ii}^{(T)}$ reveal that small scales of the scalar second-order moments completely return to isotropy for high Reynolds numbers $Re_\lambda \sim 10^3$. Moreover, it has been pointed out in experiments and DNS (Pumir 1994; Danaila *et al.* 1999) that at the level of the scalar third-order moments, some anisotropy remains in the small scales. This is not incompatible with small-scales isotropic second-order moments as shown recently by Bos (2014) in HITSG.

### 5.3. *Growth laws of the energies in HSTSG*

The HSTSG configuration is now considered at very high Reynolds numbers. As mentioned before, the kinetic energy eventually grows exponentially in shear flows at the rate $\gamma = 0.34$, defined in (4.13), within the present anisotropic EDQNM closure in a completely homogeneous framework (Mons *et al.* 2016; Briard *et al.* 2016). In this part, the emphasis is put on the growth of the scalar variance and its interactions with the

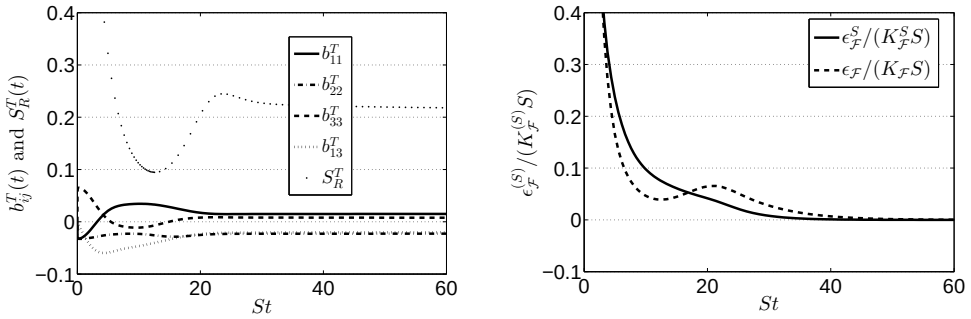


FIGURE 14. Evolution of integrated quantities in HSTSG, as a function of the accumulated anisotropy $St$, for $\sigma = 2$ and $Re_\lambda(St = 60) = 4.10^4$. At left, scalar anisotropy indicators $b_{ij}^T$ defined in (3.5), and scalar shear rapidity $S_R^T = \epsilon_T/(K_T S)$. At right, ratios $\epsilon_{\mathcal{F}}/(K_{\mathcal{F}} S)$ and $\epsilon_{\mathcal{F}}^S/(K_{\mathcal{F}}^S S)$.

scalar flux. Some additional results about the passive scalar and the scalar flux are presented, which may be of interest for one-point modelling, such as identifying negligible quantities, and their corresponding mechanisms, at high shear rates.

Firstly, the scalar anisotropy tensors $b_{ij}^T$ are presented in figure 14. As in the HST case without scalar gradient, the scalar indicators reach constant values for large $St$, and the ratio $\Lambda/S$ impacts only the short time dynamics without modifying the asymptotic state. There is a noteworthy similarity with the behaviour of $b_{ij} = R_{ij}/(2K) - \delta_{ij}/3$ in shear flows. An interesting feature is that the ratios $\epsilon_{\mathcal{F}}/(K_{\mathcal{F}} S)$ and $\epsilon_{\mathcal{F}}^S/(K_{\mathcal{F}}^S S)$ tend to zero for large $St$, whereas their kinetic and scalar counterparts do not. This means that the linear effects of shear are preponderant over non-linear exchanges at the scalar flux level: this is in agreement with figure 8, where the scalar flux transfers of energy are gathered at large scales, dominated by linear mechanisms. The evolution of the scalar, cospectrum and streamwise flux energies are given by

$$\frac{dK_T}{dt} = 2\Lambda K_{\mathcal{F}} - \epsilon_T \tag{5.8}$$

$$\frac{dK_{\mathcal{F}}}{dt} = \Lambda R_{33} + \Pi_{\mathcal{F}} - \epsilon_{\mathcal{F}} \tag{5.9}$$

$$\frac{dK_{\mathcal{F}}^S}{dt} = \Lambda R_{13} + SK_{\mathcal{F}} + \Pi_{\mathcal{F}}^S - \epsilon_{\mathcal{F}}^S, \tag{5.10}$$

where $K_T$, $K_{\mathcal{F}}$ and $K_{\mathcal{F}}^S$ have been respectively defined in (3.6), (4.4) and (4.18). Here is what happens simultaneously: the cross-correlation $R_{13}$ produces $K_{\mathcal{F}}^S$ through the mean scalar gradient $\Lambda$. $R_{13}$ brings energy to the transverse component $R_{33}$ thanks to non-linear redistribution, which causes $K_{\mathcal{F}}$ to grow as well through $\Lambda$. Finally, $K_{\mathcal{F}}$ provokes the growth of $K_T$. The main result, displayed in figure 15, is that the scalar variance $K_T$, which was exponentially decreasing in HST, now grows exponentially in HSTSG. Its scalar growth rate is $\gamma_T = \gamma = 0.34$. This is qualitatively in agreement with the experimental work of Ferchihi & Tavoularis (2002), where the scalar variance and kinetic energy grow exponentially at the same rate in the presence of both mean velocity and scalar gradients. Moreover, both the cospectrum energy $K_{\mathcal{F}}$ and the streamwise flux energy $K_{\mathcal{F}}^S$ grow exponentially with the rate $\gamma$ as well. This is consistent with the constant scalar flux correlations $\rho_{u_i\theta}$ obtained in §4 for sufficiently high $St$. From the equations (5.10), it is possible to determine the analytical expressions of the cospectrum, streamwise flux and scalar exponential growth rates $\gamma_{\mathcal{F}}$, $\gamma_{\mathcal{F}}^S$ and $\gamma_T$. Using the fact that

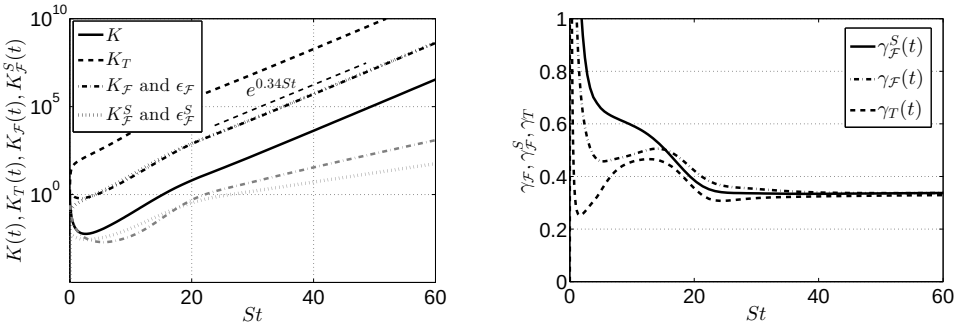


FIGURE 15. Evolution of integrated quantities in HSTSG, as a function of the accumulated anisotropy $St$, for $\sigma = 2$ and $Re_\lambda(St = 60) = 4.10^4$. At left, exponential growth of the kinetic, scalar, cospectrum and streamwise flux energies. The cospectrum and streamwise flux dissipation rates $\epsilon_{\mathcal{F}}$ and $\epsilon_{\mathcal{F}}^S$ are displayed in grey. At right, the exponential growth rates $\gamma_{\mathcal{F}}$, $\gamma_{\mathcal{F}}^S$ and $\gamma_T$.

$\epsilon_{\mathcal{F}}/(K_{\mathcal{F}}S) \to 0$ and $\epsilon_{\mathcal{F}}^S/(K_{\mathcal{F}}^S S) \to 0$, one has

$$\frac{1}{K_{\mathcal{F}}S}\frac{dK_{\mathcal{F}}}{dt} = \underbrace{\frac{\Lambda}{S}\frac{R_{33}}{K_{\mathcal{F}}} + \frac{\Pi_{\mathcal{F}}}{K_{\mathcal{F}}S}}_{\text{Constant for } St \gg 1} = \gamma_{\mathcal{F}}, \tag{5.11}$$

$$\frac{1}{K_{\mathcal{F}}^S S}\frac{dK_{\mathcal{F}}^S}{dt} = \underbrace{\frac{K_{\mathcal{F}}}{K_{\mathcal{F}}^S}(1 + Pr_T) + \frac{\Pi_{\mathcal{F}}^S}{K_{\mathcal{F}}^S S}}_{\text{Constant for } St \gg 1} = \gamma_{\mathcal{F}}^S, \tag{5.12}$$

$$\frac{1}{K_T S}\frac{dK_T}{dt} = \underbrace{2\frac{\Lambda}{S}\frac{K_{\mathcal{F}}}{K_T} - \frac{\epsilon_T}{K_T S}}_{\text{Constant for } St \gg 1} = \gamma_T. \tag{5.13}$$

The agreement between the asymptotic values of these quantities and the 0.34 expected is presented in figure 15. Moreover, simulations show that $\gamma_{\mathcal{F}}$, $\gamma_{\mathcal{F}}^S$ and $\gamma_T$ do not depend on large scales initial conditions $\sigma$. All the results regarding the exponential rates of the energies and their dissipation rates in HST and HSTSG are gathered in Table 5.

### 5.4. *Discussion on the streamwise flux spectrum $\mathcal{F}_S(k,t)$ scaling*

The scaling of the streamwise flux $\mathcal{F}_S$ is now addressed. This is of particular interest since $< u_1\theta >$ only exists when both mean velocity and scalar gradients are active, such as in atmospheric flows. Wyngaard & Coté (1972) firstly proposed

$$\mathcal{F}_S(k,t) \sim \Lambda S k^{-3}. \tag{5.14}$$

by assuming that $\mathcal{F}_S$ depends on $\epsilon$, $k$, $S$ and $\Lambda$ (this expression can also be found starting from $\mathcal{F}_S \sim \Lambda\epsilon^{1/3}k^{-7/3}$ and replacing $\epsilon^{1/3}$ by its expression as a function of the shear scale $\epsilon^{1/3} \sim k^{-2/3}S$). This is not satisfactory as there is no dependence on $\epsilon$. In a recent paper, Knaus & Pantano (2009) studied reactive and non-reactive scalar flux spectra with DNS and found that a $k^{-7/3}$ range was a satisfactory behaviour. Such a scaling

$$\mathcal{F}_S(k,t) \sim S\epsilon^{-2/3}\epsilon_{\mathcal{F}}^S k^{-7/3}.$$

assumes that $\epsilon_{\mathcal{F}}^S$ is conserved, which is false since $\mathcal{F}_S$ is purely anisotropic and does not exist in HIT. With the present modelling, it is revealed in figure 16 that there is a good agreement with the $k^{-23/9}$ scaling predicted by Bos & Bertoglio (2007)

$$\mathcal{F}_S(k,t) = C_{\mathcal{F}}^S\,\Lambda\,S^{1/3}\,\epsilon^{2/9}\,k^{-23/9}. \tag{5.15}$$

| | Exp. rates $\forall(S,\sigma,\sigma_T)$ in HST | Exp. rates $\forall(S,\Lambda,\sigma)$ in HSTSG |
|---|---|---|
| $K(t)$ | $\gamma = 2b_{13} - \epsilon/KS = 0.34$ | $\gamma = 0.34$ |
| $\epsilon(t)$ | $\gamma$ | $\gamma$ |
| $L(t)$ | $\gamma/2$ | $\gamma/2$ |
| $K_T(t)$ | $\gamma_T = \epsilon_T/K_T S = -0.52$ | $\gamma_T = (2\Lambda K_\mathcal{F})/(SK_T) - \epsilon_T/(K_T S) = 0.34$ |
| $\epsilon_T(t)$ | $\gamma_T$ | $\gamma_T$ |
| $L_T(t)$ | $\gamma/2$ | $\gamma/2$ |
| $K_\mathcal{F}(t)$ | not defined | $\gamma_\mathcal{F} = (\Lambda R_{33})/(SK_\mathcal{F}) + \Pi_\mathcal{F}/(K_\mathcal{F} S) = 0.34$ |
| $K^S_\mathcal{F}(t)$ | not defined | $\gamma^S_\mathcal{F} = (K_\mathcal{F}/K^S_\mathcal{F})(1 + Pr_T) + \Pi^S_\mathcal{F}/(K^S_\mathcal{F} S) = 0.34$ |
| $\epsilon_\mathcal{F}(t)$ | not defined | $\ll \gamma_\mathcal{F}$ |
| $\epsilon^S_\mathcal{F}(t)$ | not defined | $\ll \gamma^S_\mathcal{F}$ |

TABLE 5. Exponential rates of integrated quantities for the velocity, passive scalar and scalar flux fields in HST and HSTSG. $\sigma$ and $\sigma_T$ are the kinetic and scalar infrared slopes. $S$ and $\Lambda$ are the mean velocity and scalar gradients. $\gamma$, $\gamma_T$, $\gamma_\mathcal{F}$ and $\gamma^S_\mathcal{F}$ are the exponential rates of $K$, $K_T$, $K_\mathcal{F}$ and $K^S_\mathcal{F}$ respectively. The definitions of the kinetic and scalar integrated quantities are recalled in Table 3. For the scalar flux: cospectrum energy $K_\mathcal{F} = \int \mathcal{F}\, dk$; streamwise flux energy $K^S_\mathcal{F} = \int \mathcal{F}_S\, dk$; cospectrum energy dissipation rate $\epsilon_\mathcal{F} = (\nu + a)\int k^2 \mathcal{F}\, dk$; and the streamwise flux energy dissipation rate $\epsilon^S_\mathcal{F} = (\nu + a)\int k^2 \mathcal{F}_S\, dk$.

Numerically, the constant is found to be $C^S_\mathcal{F} \simeq 1.5$. This scaling relies on the assumption that one needs to take into account anisotropy for the form of the dissipation rate $\epsilon$. Starting with the scaling of the cospectrum, $\epsilon^{1/3}$ is replaced by $\epsilon^{1/3}_{ij}(k)$ so that

$$F_i(k,t) \sim \lambda_j \epsilon^{1/3}_{ij} k^{-7/3}. \tag{5.16}$$

Then, one has $\epsilon_{ij}(k)E(k) = 3\phi_{ij}(k)\epsilon$, where $\phi_{ij}$ is the spherical average of the spectral Reynolds tensor. The $k^{-23/9}$ law is recovered using the scaling proposed by Lumley (1967) $\phi_{13} \sim S\epsilon^{1/3}k^{-7/3}$.

### 5.5. *Return to isotropy in HSTSG*

The small scales RTI is finally addressed for the HSTSG configuration, at the level of the scalar second-order moments. In figure 17, the scalar anisotropy tensors $H^{(T)}_{ij}$ are presented at large $St$ at two different Reynolds numbers: local isotropy is recovered for the diagonal components of $H^{(T)}_{ij}$ which are zero at small scales, whereas the extra-diagonal component $H^{(T)}_{13}$ shows that some residual anisotropy still remains at small scales. This confirms that in the presence of shear, and in agreement with most of the DNS and experiments, some anisotropy persists at the scalar small scales, even at the second-order moments level. Furthermore, the Reynolds number is found to have a non-negligible impact on the small scales anisotropy, as previously noticed by Garg & Warhaft

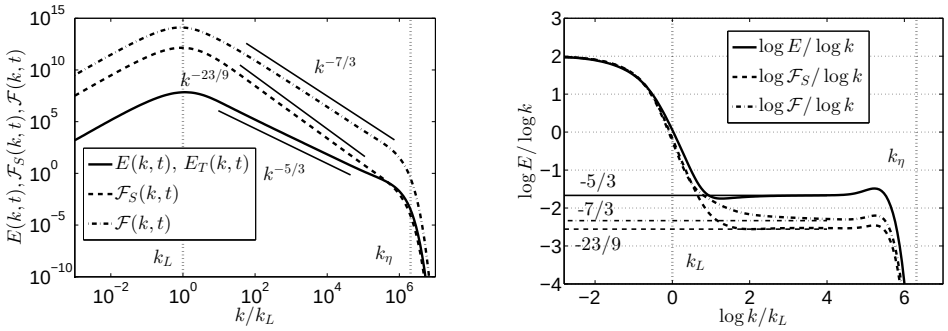


FIGURE 16. At left, kinetic, cospectrum and streamwise flux spectra $E$, $\mathcal{F}$ and $\mathcal{F}_S$, as a function of the normalized wavenumber $k/k_L$. At right, associated spectral scaling: the horizontal dashed lines correspond to $-5/3$, $-7/3$, $-23/9$, as a function of the normalized wavenumber $\log k/k_L$. Both at $St = 60$, where $Re_\lambda = 4.10^4$, and $\sigma = 2$.

(1998) for the velocity field: indeed, the reduction of small scale anisotropy, especially for $H_{13}^{(T)}$, is noteworthy from $Re_\lambda = 2400$ (already higher than the $Re_\lambda$ reached in DNS) to $Re_\lambda = 2.10^4$. The shear wavenumber $k_S = \sqrt{S^3/\epsilon}$ (Corrsin 1958) is displayed as well: for wavenumbers $k > k_S$, non-linear effects are dominant, consistent with the RTI of small scales, whereas for $k < k_S$, linear effects are stronger and carry most of the anisotropy. A last remark is that the scalar gradient seems to smooth the scalar large scale anisotropy: indeed, for shear-driven flows without mean scalar gradient, anisotropy is gathered around the scalar peak of energy $k_T$ and is weaker in the infrared range (see figure 6). Whereas for HSTSG, anisotropy progressively increases from moderate to large scales.

Therefore, the conclusion about the return to isotropy of a passive scalar small scales is twofold. Firstly, and consistently with what is observed for shear flows, an increasing Reynolds number is found to reduce small scale anisotropy for the scalar second-order moments. Nevertheless, some anisotropy remains even at the highest Reynolds numbers reached here ($\sim 10^4$). Secondly, simulations indicate that, at high Reynolds numbers, scalar small scales are still slightly anisotropic in shear-driven flows (with or without an additional mean scalar gradient). Whereas they completely return to isotropy when there is only a mean scalar gradient.

## 6. Conclusion

This study aims at modelling a passive scalar field and its associated scalar flux in homogeneous anisotropic turbulence (HAT). This work is an extension of the modelling developed in Mons *et al.* (2016) which is devoted to the velocity field. A similar two-steps approach, that could be called *anisotropic EDQNM closure*, was consistently applied here. Firstly, dynamical equations that govern the passive scalar and scalar flux fields were closed using a quasi-normal approximation and an isotropic eddy-damping procedure without any assumption regarding anisotropy. Then, for moderately anisotropic flows, scalar spherically-averaged descriptors that depend only on the wavenumber modulus $k$ were presented. Consequently, the dynamics of the velocity, passive scalar and scalar flux fields is described by six generalized spherically-averaged Lin equations: three for the velocity field, two for the passive scalar, and one for the scalar flux. The last three ones, (3.7), (3.8) and (3.9), represent the first theoretical contribution of this work. These equations are valid for arbitrary mean velocity and scalar gradients of moderate intensity.

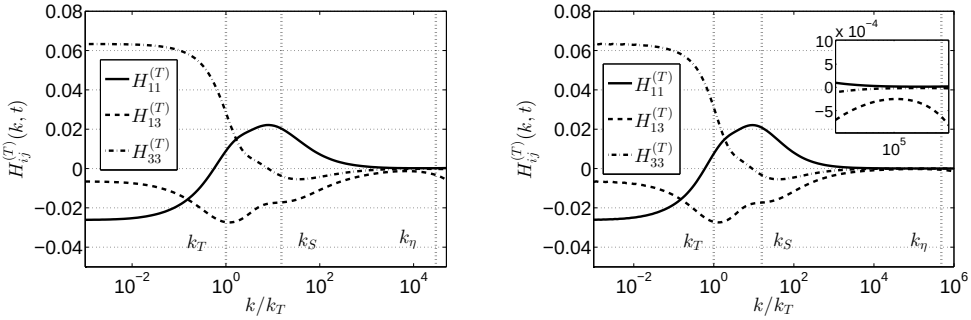


FIGURE 17. Scalar anisotropy descriptors $H_{ij}^{(T)}$, defined in (3.3), along with the Kolmogorov, shear and scalar integral wavenumbers $k_\eta$, $k_S = \sqrt{S^3/\epsilon}$ and $k_T$, for $\sigma = 2$, at two different Reynolds numbers, as a function of the normalized wavenumber $k/k_T$. At left, $Re_\lambda(St = 40) = 2400$. At right, $Re_\lambda(St = 50) = 2.10^4$. The zoom represents the small scales before $k_\eta$ where anisotropy persists.

Three different homogeneous configurations are considered in this work, whose comprehension is crucial to understand the dynamics of complex flows such as atmospheric ones: isotropic turbulence with a mean scalar gradient (HITSG), shear turbulence (HST) and shear turbulence with a scalar gradient (HSTSG). The anisotropic EDQNM modelling is assessed by detailed comparisons with several DNS and experiments at moderate Reynolds numbers in HITSG and HSTSG: asymptotic values of scalar flux correlations, turbulent Prandtl numbers and diffusivity tensors are well recovered, and the agreement at short time is satisfactory as well.

Then, the model is used to address high Reynolds numbers flows which are not accessible by DNS yet. In HITSG, the scalar flux along the mean scalar gradient, the cospectrum $\mathcal{F}(k,t)$, is found to scale as $k^{-7/3}$ in the inertial range for very large Reynolds numbers $Re_\lambda \geqslant 10^4$. New results are proposed regarding the decay and growth of $< u_3\theta >$ and $< \theta\theta >$: theoretical exponents are derived using physical arguments, and are then assessed numerically. Such results were not provided before and complete the work of Chasnov (1995). This is the second theoretical contribution of this work, that provides further insights into the prediction of high Reynolds numbers decaying turbulence. In HSTSG, the spectral scaling of the streamwise flux $\mathcal{F}_S(k,t)$ in $k^{-23/9}$ is recovered (Bos & Bertoglio 2007), and alternative scaling are briefly discussed. The interesting result of this part is the exponential growth of the passive scalar and scalar flux energies, at a rate equal to the one of the kinetic energy. In these three configurations, the small scales return to isotropy of scalar second-order moments was investigated. Numerical simulations show that scalar small scales return completely to isotropy in HITSG, which is not surprising since the velocity field remains isotropic. On the contrary, when there is a mean velocity gradient (with or without an additional mean scalar gradient), some anisotropy persists in the scalar small scales even at high Reynolds numbers, which is consistent with DNS and experiments. This small scale anisotropy for the passive scalar is found to diminish with an increasing Reynolds number.

Rotation was not investigated in this work, because its effects on triple correlations are not clear, and as mentioned in the introduction, interacting waves require additional theoretical tools, such as EDQNM2 (Cambon & Jacquin 1989; Sagaut & Cambon 2008), to be properly captured. It is nevertheless a necessary step to the deep understanding of atmospheric flows: the DNS by Brethouwer (2005) suggests that the effects of a rotating shear on the passive scalar transport and its flux are multiple and rather complex. Fi-

nally, the present modelling could be easily applied to unstably stratified homogeneous turbulence (USHT), since stratification amounts only to additional linear transfers, much simpler than the ones induced by mean-velocity gradients. USHT was recently investigated by Burlot *et al.* (2015) with a different anisotropic EDQNM approach, without reduction in terms of spherically-averaged descriptors: the linear parts (of the $\boldsymbol{k}$-dependent Craya equations) are exactly computed, but the numerical integration of the non-linear transfers require huge computational resources.

In conclusion, this anisotropic EDQNM modelling seems promising since it recovers quite well previous experimental and numerical results, and additionally permits to explore large Reynolds numbers. It can predict the velocity and scalar fields dynamics for various kinds of anisotropy with the same consistent method and does not rely on adjustable constants, except the classical ones used in the eddy-damping factors. The objective of this ongoing work is to provide a complete mapping of the scalar field in HAT with three parameters: the shear rate $S$, the scalar gradient $\Lambda$, and the Prandtl number $Pr$, whose effects on the passive scalar dynamics will be the subject of a next study.

## Acknowledgments

The authors are grateful to V. Mons for valuable discussions.

## Appendix A. Scalar infrared slope

In this part, some details are given to explain why there is no loss of generality when the infrared kinetic and scalar slopes $\sigma$ and $\sigma_T$ are chosen equal. The scalar gradient $\Lambda$ results in a production term in the passive scalar equation. This scalar production is linked to the cospectrum, itself linked to the kinetic energy spectrum. Hence, the "minimum of energy" of the flow is imposed by the infrared range of the kinetic spectrum (*i.e.* imposed by $\sigma$). So, the scalar infrared exponent $\sigma_T$ changes if initially different from $\sigma$.

For instance, if $\sigma_T(t=0) > \sigma$, this rapidly results into $\sigma_T = \sigma$. Indeed, $\sigma_T > \sigma$ means $K_T < K$: as the kinetic field imposes the minimum of energy, $\sigma_T$ will decrease down to $\sigma$. For instance, if one has $\sigma_T(t=0) = 4$ and $\sigma = 2$, the self-similar regime is $\sigma = \sigma_T = 2$ (and so for this flow $p_T = 0$).

Similarly, if $\sigma_T < \sigma$, then $\sigma_T = \sigma$ but it takes more time, as revealed in figure 18. Once again, this is because of the velocity field. Without the scalar gradient, the scalar variance would decrease, slower than the kinetic energy. The production term being proportional to $K(t)$, it forces the scalar field to grow with the infrared slope $\sigma_T = \sigma$.

## Appendix B. Additional comparison

Here, for historical reasons, simulations are compared to the experiment of Tavoularis & Corrsin (1981) which was one of the first experiments to deeply investigate the HSTSG configuration. The mean speed is $U_c = 12.4 m.s^{-1}$ and the characteristic length is the shear generator one $h = 0.305m$. The velocity gradient is $dU_1/dx_2 = 46.8 m.s^{-1}$ and the scalar one $dT/dx_2 = 9.5°C.m^{-1}$. From the data of the kinetic characteristic time written $\tau_u = 2\tau_0 = 0.26s$, $S = 6.19\tau_0^{-1}$ is found. Then, from the scalar characteristic time $\tau_\theta$ and the mean scalar fluctuations $< \theta^2 >$ it is possible to compute the reference scalar gradient. Let's mention that initial isotropic conditions are used, which is clearly not the case in the experiment. Two final Reynolds numbers are proposed: $R_{\lambda_g} = 160$ scaled for

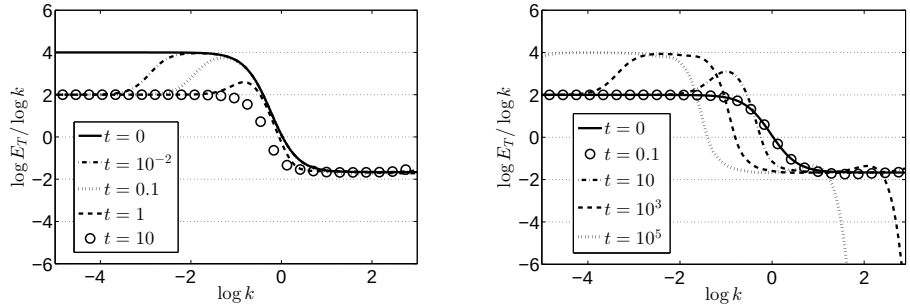


FIGURE 18. Spectral evolution of the scalar infrared slope $\sigma_T$ for $Re_\lambda(0) \sim 3.10^3$, as a function of the wavenumber $\log k$. At left, $\sigma_T(t=0) = 4$ and $\sigma = 2$. At right, $\sigma_T(t=0) = 2$ and $\sigma = 4$.

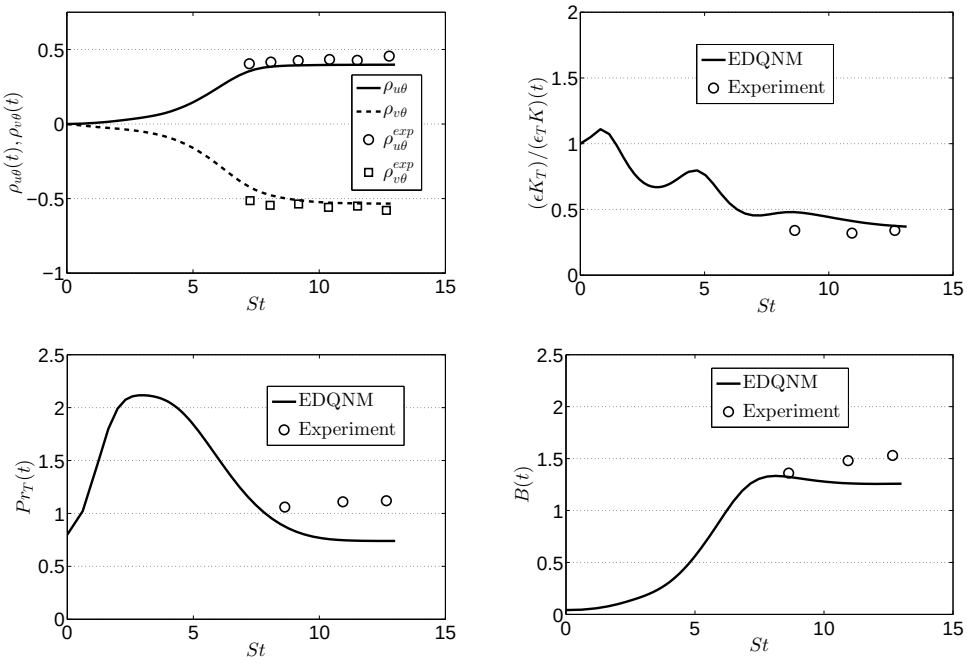


FIGURE 19. Comparisons with the experimental results of Tavoularis & Corrsin (1981), for $\sigma = 2$, $S = 6.19\tau_0^{-1}$ and $\mathcal{S}_\theta = 0.1823$, as a function of the accumulated anisotropy $St$. Top row: the scalar flux correlations $\rho_{u_i\theta}$ defined in (4.10), and the inverse of the time scales ratio defined in (4.11). Bottom row: the turbulent Prandtl number $Pr_T$ defined in (4.20) and the relative strength of the fluctuations $B = \sqrt{3}/\beta$ where $\beta$ is defined in (4.21).

isotropic turbulence, and $R_{\lambda_{11}} = 266$ for inhomogeneous flows, chosen here as it appears to be more appropriate.

The comparisons are presented in figure 19. Data is available at three locations: $x_1/h = 7.5$, 9.5 and 11. Using the appropriate conversion in dimensionless time $St = (x_1/U_c)(dU_1/dx_2)$, this provides experimental information at $St = 8.63$, 10.94 and 12.66. There are good agreements in figure 19 for the cospectrum and streamwise flux correlations $\rho_{v\theta}$ and $\rho_{u\theta}$. Similar values for $\rho_{u\theta}$ and $\rho_{v\theta}$ are reported in Ferchihi & Tavoularis (2002). There is a satisfactory agreement as well for the characteristic times ratio $\tau_\theta/\tau_u = 1/R_T$, where $R_T$ has been defined in (4.11). A first discrepancy is observed for $B(t) =$

$\sqrt{3}/\beta$, where $\beta$ has been defined in (4.21), which is underestimated in the present simulations. Let's point out that all measured quantities but $B(t)$ have converged, which is not realistic. Moreover, $B(t)$ seems to be very dependent of initial conditions, which could explain the present difference. One has to keep in mind that the initial condition is isotropic, whereas in the experiment there is initially anisotropy in the flow, difficult to model. This may explain as well the strong variations observed for $(\epsilon K_T)/(\epsilon_T K)$ at small $St$. Finally, a difference is observed for the turbulent Prandtl number, defined in (4.20), which is here $Pr_T = (\Lambda/S)(R_{12}/K_{\mathcal{F}})$. The value obtained experimentally $Pr_T^{\rm exp} \simeq 1.1$ seems quite large compared to EDQNM $Pr_T^{\rm EDQNM} \simeq 0.74$. Indeed, Herring *et al.* (1982) and Lesieur (2008) have both reported, from atmospheric data and theoretical considerations, that one should obtain $0.6 \leqslant Pr_T \leqslant 0.8$, which is in agreement with the present results. Moreover, other values of the turbulent Prandtl numbers reported from DNS and experiments agree better with 0.7 than with 1.1 (Shirani *et al.* 1981; Rogers *et al.* 1989). Let's mention that the comparison with Bos & Bertoglio (2007) for $Pr_T$ is not relevant because a constant of their model for linear transfers is set so that $Pr_T^{\rm exp} = 1.1$ is recovered.

## REFERENCES


Bos, W. J. T. 2014 On the anisotropy of the turbulent passive scalar in the presence of a mean scalar gradient. *Journal of Fluid Mechanics* **744**, 38–64.

Bos, W. J. T. & Bertoglio, J.-P. 2007 Inertial range scaling of scalar flux spectra in uniformly sheared turbulence. *Physics of Fluids* **19**.

Bos, W. J. T., Touil, H. & Bertoglio, J.-P. 2005 Reynolds number dependency of the scalar flux spectrum in isotropic turbulence with a uniform scalar gradient. *Physics of Fluids* **17**.

Bos, W. J. T., Touil, H., Shao, L. & Bertoglio, J.-P. 2004 On the behavior of the velocity-scalar cross correlation spectrum in the inertial range. *Physics of Fluids* **16**.

Brethouwer, G. 2005 The effect of rotation on rapidly sheared homogeneous turbulence and passive scalar transport. linear theory and direct numerical simulation. *Journal of Fluid Mechanics* **542**, 305342.

Briard, A., Gomez, T., Mons, V. & Sagaut, P. 2016 Decay and growth laws in homogeneous shear turbulence. *Journal of Turbulence* **17** (7), 699–726.

Briard, A., Gomez, T., Sagaut, P. & Memari, S. 2015 Passive scalar decay laws in isotropic turbulence: Prandtl effects. *Journal of Fluid Mechanics* **784**, 274–303.

Burlot, A., Gréa, B.-J., Godeferd, F. S., Cambon, C. & Griffond, J. 2015 Spectral modelling of high reynolds number unstably stratified homogeneous turbulence. *Journal of Fluid Mechanics* **765**, 17– 44.

Cambon, C. & Jacquin, L. 1989 Spectral approach to non-isotropic turbulence subjected to rotation. *Journal of Fluid Mechanics* **202**, 295–317.

Cambon, C., Jeandel, J. & Mathieu, J. 1981 Spectral modelling of homogeneous non-isotropic turbulence. *Journal of Fluid Mechanics* **104**, 247–262.

Cambon, C. & Rubinstein, R. 2006 Anisotropic developments for homogeneous shear flows. *Physics of Fluids* **18**.

Chasnov, J. R. 1995 Similarity states of turbulence asslve scalar transport in buoyancy-generated. *Physics of Fluids* **7** (7).

Comte-Bellot, G. & Corrsin, S. 1966 The use of a contraction to improve the isotropy of a grid generated turbulence. *Journal of Fluid Mechanics* **25**, 657–682.

Corrsin, S. 1958 On local isotropy in turbulent shear flow. *NACA RM 58B11* .

Danaila, L., Le Gal, P., Anselmet, F., Plaza, F. & Pinton, J. F. 1999 Some new features of the passive scalar mixing in a turbulent flow. *Physics of Fluids* **11**, 636–646.

De Marinis, D., Chibbaro, S., Meldi, M. & Sagaut, P. 2013 Temperature dynamics in decaying isotropic turbulence with joule heat production. *Journal of Fluid Mechanics* **724**, 425449.

De Souza, F. A., Nguyen, V. D. & Tavoularis, S. 1995 The structure of highly sheared turbulence. *Journal of Fluid Mechanics* **303**, 155–167.

Ferchihi, M. & Tavoularis, S. 2002 Scalar probability density function and fine structure in uniformly sheared turbulence. *Journal of Fluid Mechanics* **461**, 155182.

Garg, S. & Warhaft, Z. 1998 On the small scale structure of simple shear flow. *Physics of Fluids* **10**, 662–673.

Gomez, T., Politano, H. & Pouquet, A. 2000 Exact relationship for third-order structure functions in helical flows. *Physical Review E* **61** (5), 5321–5325.

Gonzalez, M. 2000 Asymptotic evolution of a passive scalar advected by homogeneous turbulent shear flow. *Int. J. Heat Mass Tran.* **43**, 387–397.

Gylfason, A. & Warhaft, Z. 2009 Effects of axisymmetric strain on a passive scalar field: modelling and experiment. *Journal of Fluid Mechanics* **628**, 339356.

Herr, S., Wang, L.-P. & Collins, L. R. 1996 Edqnm model of a passive scalar with a uniform mean gradient. *Physics of Fluids* **8**, 1588.

Herring, J. R., Schertzer, D., Lesieur, M., Newman, G. R., Chollet, J. P. & Larcheveque, M. 1982 A comparative assessment of spectral closures as applied to passive scalar diffusion. *Journal of Fluid Mechanics* **124**, 411–437.

Jayesh & Warhaft, Z. 1992 Probability distribution, conditional dissipation, and transport of passive temperature fluctuations in grid-generated turbulence. *Physics of Fluids A* **4**.

Kader, B. A. & Yaglom, A. M. 1991 Spectra and correlation functions of surface layer atmospheric turbulence in unstable thermal stratification. In *Fluid Mechanics and Its Applications* (ed. O. Metais & M. Lesieur), pp. 387–412. Springer Netherlands.

Karnik, U. & Tavoularis, S. 1989 Measurements of heat diffusion from a continuous line source in a uniformly sheared turbulent flow. *Journal of Fluid Mechanics* **202**, 233– 261.

Kassinos, S. C., Knaepen, B. & Carati, D. 2007 The transport of a passive scalar in magnetohydrodynamic turbulence subjected to mean shear and frame rotation. *Physics of Fluids* **19**.

Knaus, R. & Pantano, C. 2009 On the effect of heat release in turbulence spectra of non-premixed reacting shear layers. *Journal of Fluid Mechanics* **626**, 67109.

Kolmogorov, A. N. 1941 The local structure of turbulence in incompressible viscous fluid for very large reynolds numbers. *Dokl. Akad. Nauk SSSR* **30** (301).

Leith, C.E. 1971 Atmospheric predictability and two-dimensional turbulence. *J. Atmos. Sci.* **28**, 145.

Lesieur, M. 2008 *Turbulence in fluids*. Dordrecht: Springer, 4th Edition.

Lumley, J. L. 1967 Similarity and the turbulent energy spectrum. *Physics of Fluids* **10** (4), 855–858.

Meyers, J. & Meneveau, C. 2008 A functional form of the energy spectrum parametrizing bottleneck and intermittency effects. *Physics of Fluids* **20**.

Mons, V., Cambon, C. & Sagaut, P. 2016 A spectral model for homogeneous shear-driven anisotropic turbulence in terms of spherically-averaged descriptors. *Journal of Fluid Mechanics* **788**, 147–182.

Mydlarski, L. 2003 Mixed velocity–passive scalar statistics in high-reynolds-number turbulence. *Journal of Fluid Mechanics* **475**, 173203.

Mydlarski, L. & Warhaft, Z. 1998 Passive scalar statistics in high-péclet-number grid turbulence. *Journal of Fluid Mechanics* **358**, 135175.

O'Gorman, P. A. & Pullin, D. I. 2003 The velocity-scalar cross spectrum of stretched spiral vortices. *Physics of Fluids* **15**.

O'Gorman, P. A. & Pullin, D. I. 2005 Effect of schmidt number on the velocityscalar cospectrum in isotropic turbulence with a mean scalar gradient. *Journal of Fluid Mechanics* **532**, 111140.

Orszag, S.A. 1970 Analytical theories of turbulence. *Journal of Fluid Mechanics* p. 363.

Orszag, S.A. 1977 The statistical theory of turbulence. In *Fluid Dynamics* (ed. A. Balian & J.L. Peube), pp. 237–374. Gordon and Breach, New York.

Overholt, M. R. & Pope, S. B. 1996 Direct numerical simulation of a passive scalar with imposed mean gradient in isotropic turbulence. *Physics of Fluids* **8** (11), 3128–3148.

Pope, S. B. 2000 Turbulent flows. *Cambridge University Press* .

Pouquet, A., Lesieur, M., Andre, J. C. & Basdevant, C. 1975 Evolution of high reynolds number two-dimensional turbulence. *Journal of Fluid Mechanics* **77**.

Pumir, A. 1994 A numerical study of the mixing of a passive scalar in three dimensions in the presence of a mean gradient. *Physics of Fluids* **6** (6), 2118–2132.

Pumir, A. 1996 Turbulence in homogeneous shear flows. *Physics of Fluids* **8** (11), 3112–3127.

Rogers, M. M., Mansour, N. N. & Reynolds, W. C. 1989 An algebraic model for the turbulent flux of a passive scalar. *Journal of Fluid Mechanics* **203**, 77–101.

Sagaut, P. & Cambon, C. 2008 *Homogeneous Turbulence Dynamics*. Cambridge University Press.

Shen, X. & Warhaft, Z. 2000 The anisotropy of the small scale structure in high reynolds number ($r_\lambda \sim 1000$) turbulent shear flow. *Physics of Fluids* **12** (11), 2976–2989.

Shirani, E., Ferziger, J. H. & Reynolds, W. C. 1981 Mixing of a passive scalar in isotropic and sheared homogeneous turbulence. *NASA Report No. Tf-15* **NASA-CR-164938**.

Sirivat, A. & Warhaft, Z. 1983 The effect of a passive cross-stream temperature gradient on the evolution of temperature variance and heat flux in grid turbulence. *Journal of Fluid Mechanics* **128**, 323– 346.

Speziale, C. G., Sarkar, S. & Gatski, T. B. 1990 Modeling the pressure-strain correlation of turbulence - an invariant dynamical systems approach. *NASA contractor report* (181979).

Sreenivasan, K. R. 1991 On local isotropy of passive scalars in turbulent shear flows. *Proceedings: Mathematical and Physical Sciences* **434**, 165–182.

Sreenivasan, K. R., Antonia, R. A. & Britz, D. 1979 Local isotropy and large structures in a heated turbulent jet. *Journal of Fluid Mechanics* **94**, 745–775.

Sreenivasan, K. R. & Tavoularis, S. 1980 On the skewness of the temperature derivative in turbulent flows. *Journal of Fluid Mechanics* **101**, 783–795.

Tavoularis, S. & Corrsin, S. 1981 Experiments in nearly homogenous turbulent shear flow with a uniform mean temperature gradient. part 1. *Journal of Fluid Mechanics* **104**, 311–347.

Venkataramani, K. S. & Chevray, R. 1978 Statistical features of heat transfer in grid-generated turbulence: constant-gradient case. *Journal of Fluid Mechanics* **86**, 513–543.

Waleffe, F. 1992 The nature of triad interactions in homogeneous turbulence. *Physics of Fluids* **4**, 350–363.

Warhaft, Z. 1980 An experimental study of the effect of uniform strain on thermal fluctuations in grid-generated turbulence. *Journal of Fluid Mechanics* **99**, 545–573.

Watanabe, T. & Gotoh, T. 2007 Scalar flux spectrum in isotropic steady turbulence with a uniform mean gradient. *Physics of Fluids* **19**.

Wyngaard, J. C. & Coté, O. R. 1972 Cospectral similarity in the atmospheric surface layer. *Quart. J. R. Met. Soc.* **98**, 590–603.